This paper has to be cited as: *Ezquerro, P., Tomás, R., Béjar-Pizarro, M., Fernández-Merodo, J.A., Guardiola-Albert, C., Staller, A., Sánchez-Sobrino, J.A. & Herrera, G. 2019. Improving multi-technique monitoring using Sentinel-1 and Cosmo-SkyMed data and upgrading groundwater model capabilities. Science of The Total Environment, 134757, doi: https://doi.org/10.1016/j.scitotenv.2019.134757.* The final publication is available at Elsevier via: https://doi.org/10.1016/j.scitotenv.2019.134757

Improving multi-technique monitoring using Sentinel-1 and Cosmo-SkyMed data and upgrading groundwater model capabilities

Ezquerro, P.[1,2,9], Tomás, R.[1,2,3,5], Béjar-Pizarro, M.[1,2,3], Fernández-Merodo, J.A.[1,2,3], Guardiola-Albert, C. [1,2,6], Staller, A.[7], Sánchez-Sobrino, J.A.[8], Herrera, G.[1,2,3,4]

1 Geohazards InSAR Laboratory and Modeling Group (InSARlab), Geoscience Research Department, Geological Survey of Spain (IGME), Alenza 1, 28003 Madrid, Spain; p.ezquerro@igme.es, g.herrera@igme.es, m.bejar@igme.es, jose.fernandez@igme.es, c.guardiola@igme.es
2 Spanish Working Group on Ground Subsidence (SUBTER), UNESCO, 03690 Alicante, Spain; roberto.tomas@ua.es
3 Research Partnership Unit IGME-UA on Radar Interferometry Applied to Ground Deformation (UNIRAD), University of Alicante, P.O. Box 99, 03080 Alicante, Spain
4 Earth Observation and Geohazards Expert Group (EOEG), EuroGeoSurveys, the Geological Surveys of Europe, 36-38, Rue Joseph II, 1000 Brussels, Belgium
5 Departamento de Ingeniería Civil, Escuela Politécnica Superior, Universidad de Alicante, P.O. Box 99, 03080 Alicante, Spain.
6 Environmental Geology and Geomathematics, Geoscience Research Department, Geological Survey of Spain (IGME), Alenza 1, 28003 Madrid, Spain
7 Universidad Politécnica de Madrid. Departamento de Ingeniería Topográfica y Cartografía, ETSI Topografía, Geodesia y Cartografía. Campus Sur, 28031 Madrid, Spain. a.staller@upm.es
8 Instituto Geográfico Nacional (IGN), Geodesy Department
9 Universidad Politécnica de Madrid. ETSI Caminos, Canales y Puertos C/ Profesor Aranguren s/n, 28040 Madrid, Spain

Abstract

Aquifer-systems have become a strategic source of fresh water in the present climatic conditions, especially under stress in arid regions like the Iberian Mediterranean Arc. Understanding the behavior of groundwater reservoirs is crucial to their well-management and mitigation of adverse consequences of overexploitation. In this work, we use space geodetic measurements from satellite interferometric synthetic aperture radar (InSAR) and Global Positioning System (GPS) data, covering the period 2011 – 2017, to predict and validate the ground surface displacement over the fastest subsiding basin due to groundwater withdrawal in Europe (>10 cm/year). The 2D decomposition of InSAR displacements from Cosmo-SkyMed and Sentinel-1 satellites allows us to detect horizontal deformation towards the basin center, with a maximum displacement of 1.5 cm/year. InSAR results were introduced in a newly developed methodology for aquifer system management to estimate unknown pumping rates for the 2012 – 2017 period. This study illustrates how the combination of InSAR data, groundwater flow and deformation models can be used to improve the aquifer-systems sustainable management.

Keywords

InSAR, Subsidence, Groundwater Extraction, Aquifer Management

1 Introduction

Land subsidence due to groundwater withdrawal is the response of an aquifer-system to the decrease of pore pressure (Terzaghi, 1925) and one of the main geological hazards involving flat areas with unconsolidated sediments worldwide (Motagh et al., 2008; Zhang et al., 2014; Chaussard et al., 2014a; Minderhoud et al., 2015). The consequences of this phenomenom are even more acute in areas affected by both subsidence and sea level rise problems (Erkens et al., 2015; Vousdoukas et al., 2017). These areas are usually densely populated, dedicated to agricultural uses and crossed by several infrastructures, making them especially vulnerable to surface deformation (Tomás et al., 2011; Raspini et al., 2013). Therefore, this issue has taken more relevance in a global climate change context with predicted intensive water resource scarcity, when aquifer-systems become a strategical resource of fresh water during dry seasons (EU, 2017; Wada et al., 2014). Unmanaged exploitation of groundwater reservoirs has led to reservoir depletion, saline intrusion and land subsidence, generating important social and economic impact (Hu et al., 2009; Ge et al., 2014; Alfarrah et al., 2018). In order to prevent major problems authorities in charge and water management entities are starting to increase their interest in displacement monitoring methodologies.

The Alto Guadalentín basin is located in the Mediterranean SE coast of Spain, a vulnerable area very prone to dry periods. The Spanish Mediterranean Arc has suffered three important droughts between 1990 and 2012 (CHS, 2014), and is nowadays being affected by a strong dry period lasting more than four years. The Spanish Meteorological State Agency carries out the monthly update of meteorological drought publishing the maps and reports (http://www.mapama.gob.es). Growing agricultural activities since 1960s increased the pressure over hydrological resources and led the aquifer-system management authorities to declare it as partially overexploited, supervise and regulate its use in order to stabilize the piezometric levels (CHS, 2006). Intensive overexploitation of the aquifer-system generated a severe subsidence previously studied by several authors using different SAR datasets covering the period 1992-2012 (González et al., 2011; Rigo et al., 2013; Bonì et al., 2015). Subsidence rates, the highest one measured in Europe related to groundwater withdrawal, show a slight decay from -12 cm/year in the ERS 1/2 data (1992-2000) to -10 cm/year in the Cosmo-SkyMed data (2011-2012) (Bonì et al., 2015). These radar results are supported by the Global Navigation Satellite System (GNSS) permanent stationslocated in the deformed area. Continuously declining groundwater levels since the early 1960s, have been partially stabilized in the last years, opening up new horizons in the aquifer-system management.

Subsiding areas have been usually monitored using surveying techniques as leveling and borehole extensometers (Riley, 1969; Teatini et al., 2006) and GNSS (Chen et al., 2016a; Del Soldato et al, 2018). Synthetic Aperture Radar (SAR) satellites were the next advance in surface deformations monitoring, increasing the coverage and measurements density with high accuracy (Massonet et al., 1998). These measurements are referred to the Line of Sight (LOS) of the satellite and need to be projected in order to compare them with other measurements. In order to better understand the three dimensional deformation field generated by complex phenomena such as landslides, earthquakes and groundwater-related subsidence the LOS displacement field can be decompose into vertical and horizontal (East-West) components when two satellite acquisition geometries are available (Bejar-Pizarro et al., 2017a ; Hu et al., 2012; Miller et al., 2015).

We reviewed 113 papers on land subsidence due to groundwater withdrawal, finding that 43 (i.e 38.1%) focused on the detection and monitoring of the phenomenon (e.g. Motagh et al., 2008; Righini et al., 2011; Chaussard et al., 2014a; Solari et al., 2018) and 38 (i.e. 33.6%) on the correlation of detected subsidence with groundwater changes (e.g. Amelung et al., 1999; Tomás et al., 2010; Abidin et al., 2013). Aquifer-system state can be easily estimated at discrete

locations using direct information from piezometers. Usually that information is used to generate groundwater flow models to perform estimations of the global groundwater levels and compare the water change results with the measured land subsidence (Bozzano et al., 2015). The relationship between piezometric changes (i.e. effective stress) and surface deformations (i.e. strain) was analyzed to derive the skeletal storage coefficient that is used to estimate aquifer-system deformation in 13 works (e.g. Hoffman et al., 2001; Zhang et al., 2014; Ezquerro et al., 2014; Miller et al., 2015; Boni et al., 2016). Other authors use the skeletal storage (S_k) coefficient in groundwater flow models (Subsidence and Aquifer-System Compaction, SUB, and Subsidence and Aquifer-System Compaction for Water-Table Aquifers, SWT, MODFLOW Packages) to calculate aquifer-system deformation (Hoffmann et al, 2003; Harbaugh, 2005; Leake et al., 2007; Densmore et al. 2018). In these works, S_k is derived from geotechnical tests whereas deformation measurements (Interferometric Synthetic Aperture Radar, GNSS, leveling and extensometers) are used to validate the estimated deformation with the model. Other works (7) use geo-mechanical models and piezometric data to calculate the deformational behavior (Herrera et al., 2009; Tessitore et al. 2016; Ochoa-González et al., 2018). Chaussard et al. (2014b) exploits InSAR data to calibrate skeletal storage in a MODFLOW model in the 1995-2001 period, then local hydraulic head changes are calculated with InSAR data from 2006 to 2011. Chen et al. (2016b) performs the same analysis without using a MODFLOW model. Béjar-Pizarro et al. (2017b) use the same approach than the previous work to derive for the first time spatially continuous evolution of groundwater levels and aquifer-system storage. In this framework, we propose a new methodology to improve aquifer-system modelling using satellite and geodetic measurements. Multi-sensor InSAR is applied to map and monitor vertical and horizontal displacement of an aquifer-system, which are validated with GNSS data. InSAR data covering the period 2012-2017, 3D geology and the known boundary conditions of the aquifer-system are used to generate groundwater flow and deformation models capable of simulating the response of the aquifer-system. The combination of InSAR data covering the period 2012-2017 with the previously generated models allows us to estimate the pumping rates in this period.

2 Study Area

The Alto Guadalentín area is a sedimentary basin located in the southern part of the Spanish Mediterranean Arc. The climate of the area is characterized by scarce rainfalls, with an average annual of 250 mm and less than 150 mm in alternate dry years. The basin has not permanent watercourses but is regularly affected by extreme flash flood events in the main Guadalentín, Nogalte, Torrecilla and Béjar streams (Fig. 1). The continuous increase of the populations of the basin reached 107000 habitants in 2012 with a slow decreasing trend since then (data from annual census, Spanish Statistical Office).

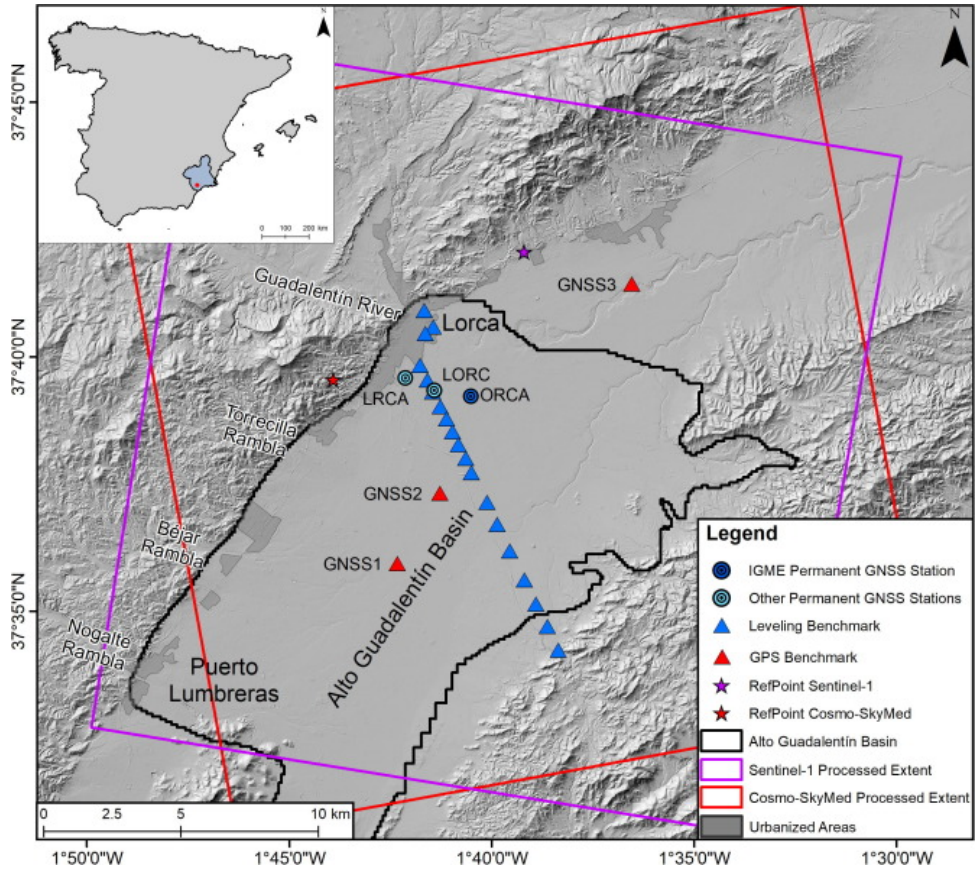

Figure 1: Alto Guadalentín study area showing the coverage of the different monitoring techniques. Top left-hand corner map represents the location of the Alto Guadalentín basin in the Murcia province, SE coast of Spain.

The orogenic tectonic depression of the Alto Guadalentín exhibits a horst and graben structure bounded to the north by the active Alhama de Murcia fault (Masana et al., 2004). Paleozoic pre-orogenic metamorphic basement reaches maximum depths of 1000 m below land surface and is covered by sedimentary materials accumulated during the basin formation. These sediments are constituted from bottom to top by Miocene marls with conglomerates and sandstones. Due to the horst and graben pattern of the bedrock, the accumulated thickness of these layers ranges from 300 to 900 m. The overlaying layers are composed by sand and gravel lenses embedded in a clay and sand matrix from the Plio-Quaternary that present a classical alluvial fan configuration (Cerón et al., 1996). Recent studies (Bonì et al., 2015) have revealed the existence of an important layer of fine grained sediments in the upper part of the Plio-Quaternary materials (Cerón, 1995) clearly correlated with the magnitude of the subsidence rate in the basin. In 2015, a new borehole drilled SW of the ORCA GNSS station (Fig. 1) allowed obtaining unaltered samples at different depths. Samples at 63 and 84 m depth showed granulometric curves with more than 98 and 65% of silt and clay fine-grained sediments, respectively. Samples at 222 m depth revealed only a 13% of fine-grained materials. Data obtained at 290 m depth returned to the high percentage of silts and clays (72%).

The most productive layer of the Alto Guadalentín Aquifer-system is linked to the Plio-Quaternary sediments, with the deep marls acting as low permeability seal (IGME, 1985). The upper part of the aquifer-system is unconfined, while deeper areas have a semi-confined behavior. Aquifer-system recharge is strongly dependent of rainfall and irrigation returns, due to the absence of permanent watercourses or positive transferences from other aquifer-systems. Recharge problems and the intensive use of underground water for agricultural purposes since 1960s led to a decline in the aquifer-system levels near 200 m in 50 years. Most

of the groundwater depletion occurred before the declaration of the aquifer-system as temporally overexploited in 1988. However, levels continued slowly decreasing in the following years due to pumping pressure and a long period of low rainfall years affecting this area and other basins that supply it during water scarcity periods through Tajo-Segura diversion (built in 1979).

Previous studies have established a relationship between groundwater changes and displacements on this aquifer-system (González et al., 2011). Using SAR images from 1992 to 2012 a continuous deformation pattern closely related with the thickness of a low and very low permeability silts and clays layer was revealed (Bonì et al., 2015). Later works presented a hydrogeological model that reproduced the groundwater evolution during the last 52 years and whose results were used to state a numerical relationship between land subsidence, water change and compressible sediments thickness (Ezquerro et al., 2017).

In order to improve previous results, during last years a complete monitoring system has been designed and implemented. A new GNSS permanent station near the maximum subsidence area was added to the two previously existing and a line belonging to the national high precision levelling network crossing the basin was reobserved. Remote sensing data over the basin were updated completing the Cosmo-SkyMed constellation dataset from 2011 to 2016 and first data from new Sentinel-1 constellation were processed assuring the continuity of the time-series during the following decade.

As presented, the study area is an important region with an historical agricultural dependence of groundwater resources. In this framework the combination of hydrogeological and surface deformation solutions are becoming an important factor to improve the groundwater management and reduce geological risks over vulnerable structures and infrastructures.

3 Methodology

3.1 Monitoring System

3.1.1 InSAR datasets and processing

Land subsidence evolution over the Guadalentín basin was measured using two different SAR images datasets from Sentinel-1 (C-band) and Cosmo-SkyMed (X-band) satellites. Sentinel-1 package is composed by forty Interferometric Wide Swath (IW) images acquired from October 2014 to July 2016 in descending orbit (track 8) (Supp. data lists of images). High temporal resolution of Sentinel-1 satellite (hereinafter referred to as S-1) allows regular image acquisition with a time span of 12 days (Torres et al., 2012). Maximum time span of 84 days was registered during the first five months of satellite operation. Cosmo-SkyMed (hereinafter referred to as CSK) dataset consists of 115 Stripmap-Himage (STR-HIMAGE) acquired from June 2011 to December 2016 in ascending orbit direction. Due to extremely high temporal resolution of CSK constellation (maximum time gap of 4 days) (Covello et al., 2010) a regular 16 days image gap has been selected in order to reduce processing machine-time costs. Spatial distribution and temporal evolution of the studied phenomenon make unnecessary the processing of the complete catalogue and the selected gap between images is short enough to reduce temporal decorrelation.

SAR images were processed using the Coherent Pixels Technique (CPT) developed by the Remote Sensing Laboratory (RSLab) at Universitat Politecnica de Catalunya (UPC) (Mora et al., 2003; Blanco-Sánchez et al., 2008; Confourto et al., 2017) and updated to S-1 TOPS acquisition system (Centolanza et al., 2017). This interferometry chain is divided into two main steps. PRISAR processing generates the co-registered images, interferograms, coherence maps and differential interferograms. SUBSOFT module is responsible for the processing of the Advanced DInSAR products, the estimation of linear and non-linear deformation components and results geocoding. Specific processing data of S-1 and CSK are summarized in Table 1.

Table 1: DInSAR processing parameters.

Satellite	**S-1**	**CSK Constellation**
Number of images	37	114
Initial date	30/10/2014	02/06/2011
Final date	03/07/2016	05/12/2016
Number of interferograms	206	323
Covered Area (km2)	625	676
Max. temporal baseline (days)	192	269
Max. spatial baseline (m)	185	488
Multilook (Az × Rg)	3 × 11	5 × 5
Number of DS	206.530	422.458

Due to the agricultural predominance of the processed area and the absence of good scatters out of the urban areas, a Small Baselines approach was selected. The maximum temporal baselines are 192 days (S-1) and 269 days (CSK) allowing a low temporal decorrelation in the interferograms. Maximum perpendicular baselines range from 185 m in S-1 to 488 m in CSK. Two of the CSK images were discarded and eliminated from the interferogram network due to their extreme temporal/perpendicular position out of the selected ranges. Based on these conditions, 206 and 323 interferograms were generated for S-1 and CSK datasets, respectively, using a multilook designed to generate a near-squared pixel with good resolution for the studied problem (3x11, about 45 m with S-1 and 5x5, 25 m with CSK).

To estimate accurate Advanced DInSAR products (Line of Sight, LOS, velocities and time series), pixels with a good quality should be selected. In this study we have used the Distributed Scatters approach (hereinafter DS), using 0.35 (S-1) and 0.40 (CSK) coherence thresholds in the initial coherent pixels candidate selection. This kind of approach fits especially well with S-1 characteristics, allowing the detection of a good point density in agricultural areas. It also improves the response of CSK data in agricultural areas, but, as clearly seen in Fig. 3, DS density is still lower than S-1 in non-urban areas. Seeds of both datasets (i.e. reference points) are located in the stable mountainous areas that surround the basin (Fig. 1). The processing of SAR data from the S-1 descending track, covering an area of 625 km^2, produced 206530 DS, while the processing of CSK ascending track data, covering an area of 676 km^2, produced 422458 DS. In both cases, the coherent pixels were mainly concentrated over urban and not vegetated areas.

Different SAR geometries (ascending and descending orbits) allow decomposing the LOS displacements into up-down and east-west components, while north-south component remains unknown due to the quasi-polar orbits of SAR satellites (Raspini et al, 2012; Notti et al., 2014).

Since our InSAR results cover the same temporal period with two different satellite viewing geometries, ascending CSK and descending S-1, there exist the possibility of calculating the above mentioned components. Due to the different spatial resolution of both satellites and results, LOS displacement rates from ascending and descending datasets were interpolated using the inverse distance weighted (IDW) method (with power 1, search radius 100 m, and three points minimum) into a final resolution of 5 m raster layer. The interpolated ascending and descending velocities were used to calculate the up-down (V_{Vert}) and east-west (V_{EW}) components of the velocity with the following formulas (Notti et al, 2014):

$$V_{EW} = \frac{\left(\left(\frac{V_d}{H_d}\right) - \left(\frac{V_a}{H_a}\right)\right)}{\left(\frac{E_d}{H_d} - \frac{E_a}{H_a}\right)} \quad (1)$$

$$V_{Vert} = \frac{\left(\left(\frac{V_d}{E_d}\right) - \left(\frac{V_a}{E_a}\right)\right)}{\left(\frac{H_d}{E_d} - \frac{H_a}{E_a}\right)} \quad (2)$$

$$H_a = \cos \alpha_a \quad (3)$$

$$H_d = \cos \alpha_d \quad (4)$$

$$E_a = \cos(90 - \alpha_a) \times \cos(270 - \gamma_a) \quad (5)$$

$$E_d = \cos(90 - \alpha_d) \times \cos(270 - \gamma_d) \quad (6)$$

Where α is the incidence angle and γ is the LOS azimuth. Subscripts a and d refer to ascending and descending parameters, respectively.

Analysis of the decomposed movements at the GNSS permanent stations were carried out using the velocities of the 80 m surrounding DSs to reduce the influence of the CSK/S-1 DS density differences and the misrepresentation of a single DS.

3.1.2 GNSS

Murcia province is monitored by two GNSS permanent stations networks managed by different departments of the Murcia Region. Due to the important seismic activity of the Lorca area in the context of the Iberian Peninsula, two permanent station (Fig. 1) belonging to the MERISTEMUM (LORC, http://gps.medioambiente.carm.es/) and REGAM (LRCA, http://sitmurcia.carm.es/web/sitmurcia/lorca) networks were installed by the regional authorities (Fig. 1). Taking into account previous subsidence studies in the area (Rigo et al., 2013; Bonì et al., 2015), LRCA GNSS station is located in a low deformation area and LORC station is on a medium subsidence area (Fig. 1).

A new GNSS permanent station (ORCA) was installed by the Spanish Geological Survey (IGME) near the maximum subsidence area. LORC data used in this study range from April 2011 to September 2017 and LRCA data range from December 2012 to September 2017. First data from the new station (ORCA) were received on 18th February 2016, finishing in September 2017. The stations are collecting 30 seconds rate data and daily RINEX files are being downloaded from the receivers to Spanish National Geographic Institute (Instituto Geográfico Nacional de España or IGN) data center.

ORCA, LORC and LRCA (Fig. 1) GNSS stations are integrated in the IBERRED project, which consists on a network covering all the country and processed by the IGN using Bernese 5.2 software (Dach et al., 2015). Most of stations of IBERRED network in Spain (about 300 stations) are also being processed by IGN for the "EUREF Dense Velocity Project" for EUREF organization (http://www.epncb.oma.be/_densification/). Post-processing methodology is based on the phase double differencing equations (Leick, 1995) using International GNSS Service (IGS) precise ephemerides (Daw et al., 2009). Daily coordinates are automatically calculated each week using

daily RINEX files with a delay of 15 days in order to use the IGS precise ephemerides. Output results are translated to local topocentric coordinates (north, east, elevation) to facilitate the interpretation.

Additionally, to complete the data of the study area, three campaign stations were established along the basin (GNSS1, GNSS2 and GNSS3) (Fig. 1). To assure the spatial-temporal stability of these stations, three concrete structures with 5/8" bolts were built. The campaign stations were observed with GPS double-frequency receivers in two campaigns developed on January 2016 and May 2017. Each station was observed at least two days with observations of at least 12 hours per day and a rate data of 15 seconds. The daily RINEX files collected were processed using Bernesse 5.2 code software (Dach et al., 2015) using a same methodology described above.

3.1.3 Surveying

Leveling is a precise and simple methods widely used to monitor subsidence (USGS, 1969; Teatini et al., 2005; Liu et al., 2013). Nowadays, this technique is often expensive and time consuming, exhibiting a high relative cost per benchmark and a low density of information (Tomás et al., 2014). For example, the surveying campaign in Lorca basin lasted 5-days for measuring 19 points (Fig. 1).

One of the nodes from the high precision leveling network of Spain (Red Española de Nivelación de Alta Precisión REDNAP) is located near Lorca city center. Four leveling lines deployed by the IGN converge on it. We focused on levelling line 10426 (from Lorca to Tébar) that crosses transversally the 13 km subsiding basin near to highest subsidence rate area. In particular, we use the stretch from the node of Lorca to the benchmark 10426/15 located over a stable area near the southwestern limit of the basin (Leveling benchmarks in Fig. 1). The orthometric height of the 16 benchmarks of this stretch was measured in March 2005 excepting Lorca node (August-September 2004) by the IGN.

On January 2016 a new measurement campaign was developed along the 13 km from Lorca node to 10426/15 benchmark. As a result of the road improvement works near the leveling line, six of the original benchmarks were destroyed. In order to repair the network for future campaigns the lost benchmarks were replaced and the original density was increased, especially over the highest subsidence area, installing nine new leveling benchmarks. Another measurement campaign was carried out on May 2017. The two levelling campaigns were measured with a LEICA SRINTER 100 digital level, using two barcode levelling staffs and levelling once in each direction with a kilometric error of 3.5 mm and a maximum tolerance in the closure error of each ring of 5 mm. Levelling campaign guarantee the determination of the vertical component in the benchmarks with an accuracy higher than of 5 mm (nominal SAR accuracy in time series). Results are calculated using the altitude difference between two benchmarks using a least squares adjustment.

3.1.4 Validation methodology

In order to validate InSAR displacement we use data gathered from different geodetic techniques acquired in different temporal periods. Due to the heterogeneity of the available in situ data we propose three different validation/comparison strategies. The first approach corresponds to the full validation, achieved when continuous GNSS stations Time Series are available to validate InSAR Time Series for the same period. The results from this comparison are the root mean squared error (RMSE) and the relative error, which is the percentage of RMSE with respect to the accumulated deformation. The second approach corresponds to the trend validation and refers to the comparison of displacement velocities measured with geodetic techniques (GNSS and Leveling) with InSAR velocities for the same period. In this case the results are the velocity error and the relative error of the velocity (%). This approach is useful when InSAR processing only provides the displacement velocity result. The third approach correspond to a trend comparison. In this case we also compare velocities, like in the previous approach,

but these velocities do not correspond to the same monitoring period. This approach is used when only historical and sparse data is available for the comparison with InSAR results.

3.2 Aquifer-system and deformation modeling using InSAR data

The proposed methodology to improve aquifer-system modeling based on InSAR data (Fig. 2) is divided into two main parts that require two different periods of data (Period 1 and 2).

The first part is based on the generation of a groundwater flow and deformation models. InSAR data (Period 1) is combined with geological data to improve the 3D geological model of the aquifer-system, by considering the spatial extent and thickness of compressible soils. This layer is combined with the boundary conditions (Period 1) of the aquifer-system to derive a groundwater flow model that allows estimating the spatial and temporal evolution of groundwater levels (Period 1). These results, together with the improved geology and InSAR data are used to elaborate a deformation model. This deformation model is then used to estimate subsidence in different temporal periods (Period 1).

In the Alto Guadalentín case study, InSAR data from the period 1992 to 2012 (Partial Period 1) was used to improve the 3D geology of the aquifer-system (Bonì et al. 2015). Then the boundary conditions available for the period 1960 to 2012 (Complete Period 1) and the improved 3D geology were used to generate a MODFLOW groundwater model for the period 1960-2012 (Complete Period 1) (Ezquerro et al. 2017). Groundwater numerical model was developed suing MODFLOW-2005 with the ModelMuse interface, both developed by the USGS (Winston, 2009). According with the input data, model time step of one year was specify. The model has three convertible layers divided in 100m grid cells. First includes the compressible fine-grained Plio-Quaternary materials. Second layer is formed by coarse-grained Plio- Quaternary sediments, representing the main aquifer layer. Third comprises Miocene low permeability material. UCODE 2014 (Poeter et al., 2014) and graphical interface ModelMate (Banta, 2011) were used to calibrate the model. The estimated groundwater evolution combined with InSAR data and the 3D Geology was used to propose a deformation model (Ezquerro et al. 2017). Empirical deformation models using linear and non-linear regressions were calculated. The quality of the models to replicate the observed data was assessed using coefficient of determination ($r2$). Most accurate model was used to estimate the deformation of the aquifer-system in the period 1960 – 2012 (Complete Period 1) when subsidence measurements were not available.

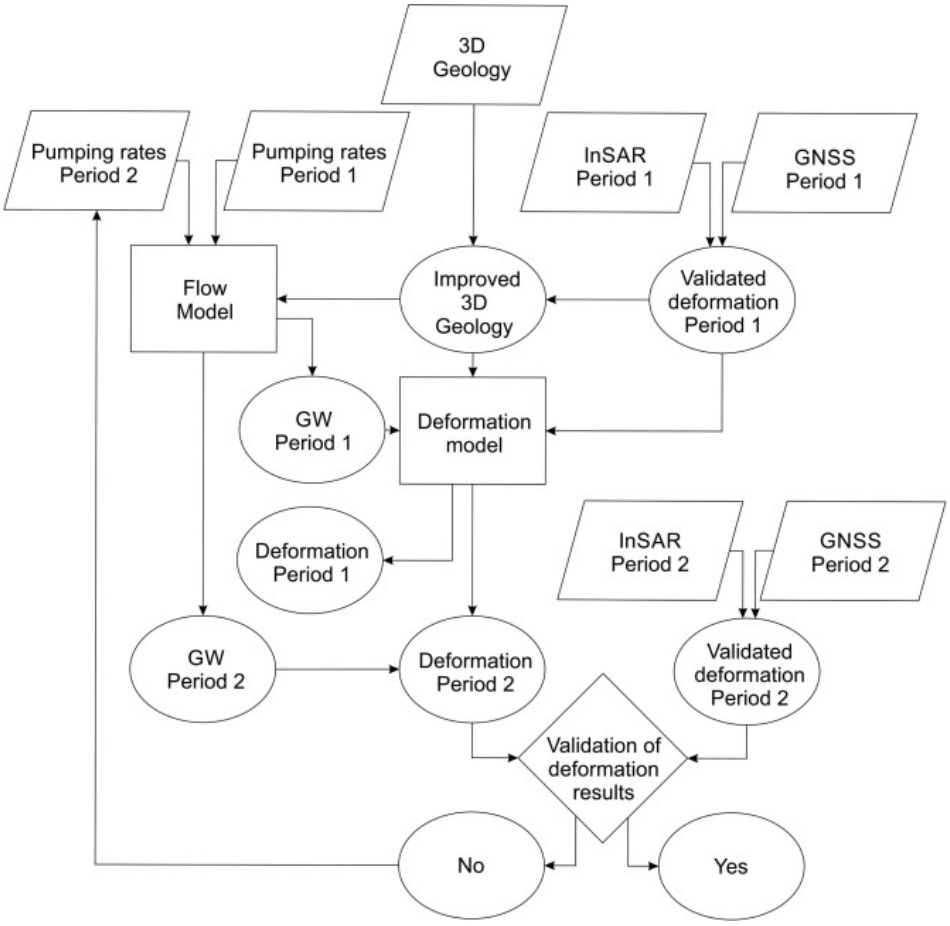

Figure 2: Flowchart used to generate the groundwater management system of the basin.

The second part takes advantage of the previously generated models and updated InSAR data (Period 2) to calculate groundwater evolution in this period and predict unknown pumping rates (Period 2). In order to do so, the available pumping rates (Period 1) are used to estimate groundwater evolution in period 2, which is then used to estimate deformation in this same period. The comparison of the estimated deformation in period 2 with the updated InSAR deformation allows calibrating the unknown pumping rates (Period 2).

In this case study, the groundwater model has been updated using the known boundary conditions for the period 2013 – 2017, calculated consistent with the formulation applied in 1961-2012 period. Infiltration is a variable percentage of rainfall (data provided by the Spanish Meteorological Agency (AEMET), Supplementary 1) between 10% in the dry years and 20% in the rainy ones using a quadratic regression curve adjusted in the 1961 to 1993 (Ezquerro et al., 2017). Lateral streams contribution use the rainfall/recharge ratio calculated for 1960 (IGME, 1994). In order to estimate groundwater evolution for the period (2013 – 2017), unknown pumping rates are assumed to be similar to those used in the first part of the methodology, where a constant extraction rate of 43 hm^3/year was introduced for the period 2005 to 2012 based on CHS (2006).

The deformation model has also been updated taking into account recent improvements in the spatial definition of the 3D geology (Béjar-Pizarro et al., 2016), and the previously used data: the estimated groundwater evolution (1960 – 2012) and the InSAR data (1992 – 2012) (Supplementary 1 & 2, respectively). We use this model to estimate deformation in the period 2013 -2017 using the previously estimated groundwater evolution for this period. The comparison of this deformation results (uncalibrated) with the CSK InSAR data available for the same period is used to perform back analysis and calibrate the unknown pumping rates. After

several iterations, the calibrated pumping rates generate a groundwater flow and a deformation result compliant with the CSK InSAR measurements.

4 Results

4.1 InSAR monitoring

Figures 3A and 3B show InSAR maps of LOS deformation rates derived from CSK and S-1 processing, respectively. We used ±1 cm/year as the stability threshold based on the standard deviation values estimated for all the DS in a stable area. Previous InSAR studies over this area revealed that radar noise over this area is usually high and stability thresholds around ±1 cm/year are consistently used (Bonì et al., 2015).

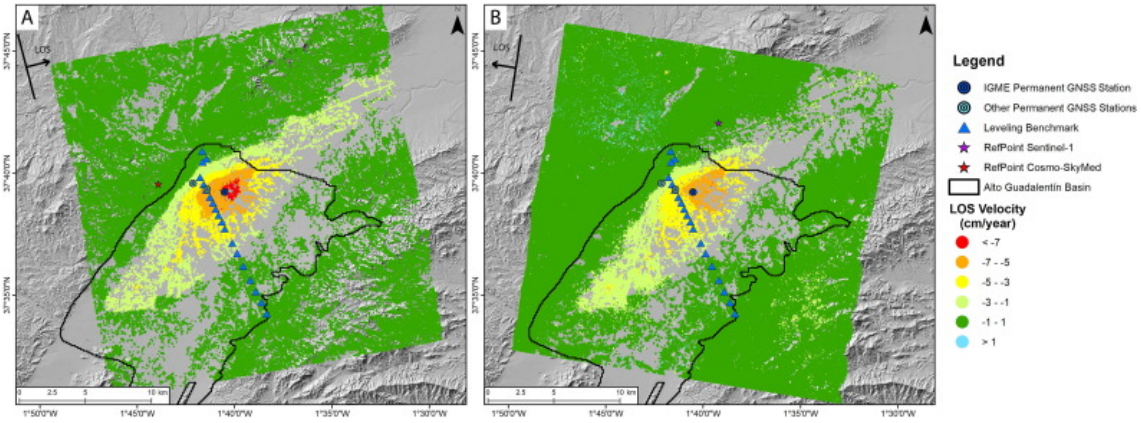

Figure 3: LOS displacement velocity in the study area for the CSK (A) and S-1 (B) datasets.

Both datasets show a similar deformation pattern with the maximum deformation area located in the northern area of the basin, near the ORCA GNSS permanent station. The maximum deformation rates detected by S-1 (November 2014 – July 2016) and by CSK (June 2011 – December 2016) were -7.5 and -8.2 cm/year, respectively. Note that both results are in LOS and should be translated into vertical displacements in order to be correctly compared. Finally, it is worth mentioning that both compared periods cover different temporal period.

Taking into account the incidence angle of both image datasets, between 37.54° and 39.08° (medium-east side of the second swath in descending orbit direction, ESA S-1 IW User guide, 2018) in S-1A data and 43.16° in CSK, vertical displacements were calculated with maximum rates of -9.7 and -11.1 cm/year for S-1A and CSK, respectively.

S-1 and CSK time series of four representative areas of the Guadalentín Valley are plotted in Figure 4C-F): A) the maximum deformation area, B) the local maximum of the southern part of the basin, C) the linking area with the Bajo Guadalentín basin in the north and D) a stable area in the NE range. It is worth noting that only the common time period between S-1 and CSK time series ranging from October 2014 to September 2016 is plotted in Figure 4A-D.

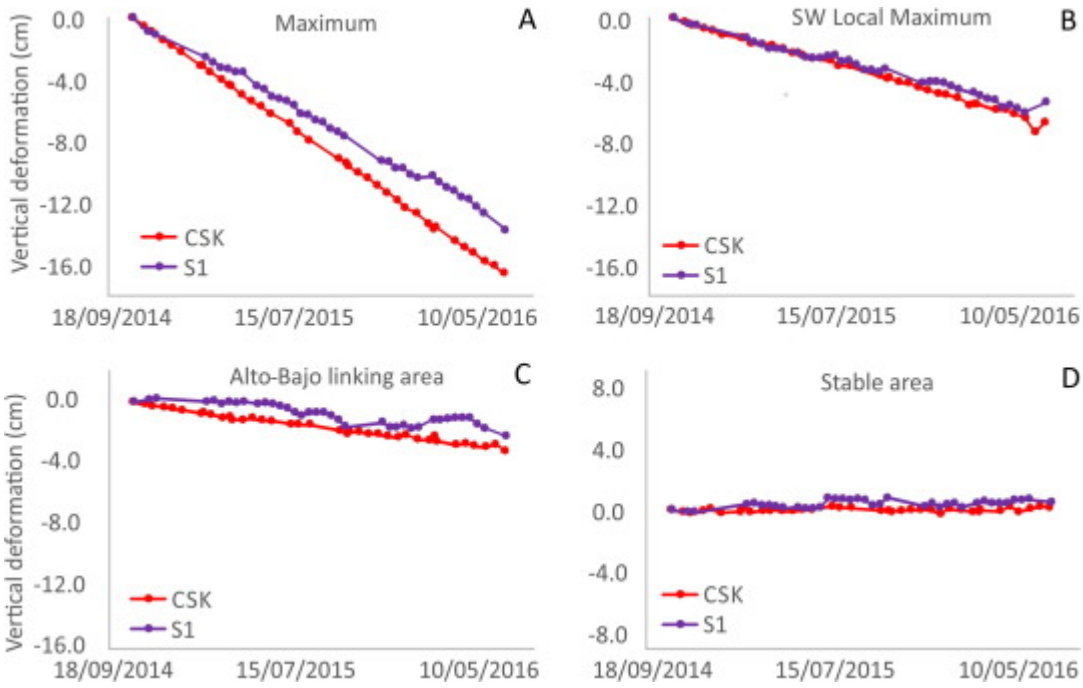

Figure 4: CSK and S-1 time series during the common time span. A) CSK/S-1 TS in the maximum subsidence area. B) CSK/S-1 TS in the SW local maximum. C) CSK/S-1 TS in the Alto-Bajo Guadalentín linking area. D) CSK/S-1 TS in an stable area lacated in the W ranges. All the data are projected along vertical direction assuming only vertical deformations.

Consistent with the spatial analysis, S-1 accumulated deformation is lower than that derived from CSK data. Maximum and linking areas are located in the central-east side of the basin where the difference is higher, meanwhile local maximum area is centered and both series are closer. Stable area displacements are under the stability threshold. S-1 time series present a high instability especially in the areas with low deformation due to the short processed time-span.

4.2 GNSS monitoring

Continuous displacement of three permanent GNSS stations were used to calculate 15 days moving average displacements to obtain more stable GNSS series. Deformation results are presented in Fig. 5, showing a general subsiding trend with higher rates towards the center of the basin in agreement with InSAR results. Average subsidence velocity of LRCA, the nearest GNSS to the basin border, is -2.75 cm/year, increasing to -7.46 cm/year in the LORC GNSS located 1.2 km towards the maximum deformation area. Over this area, deformation in ORCA is -8.42 cm/year. This time series is only 1.5 years length and, therefore, its results are still slightly unstable.

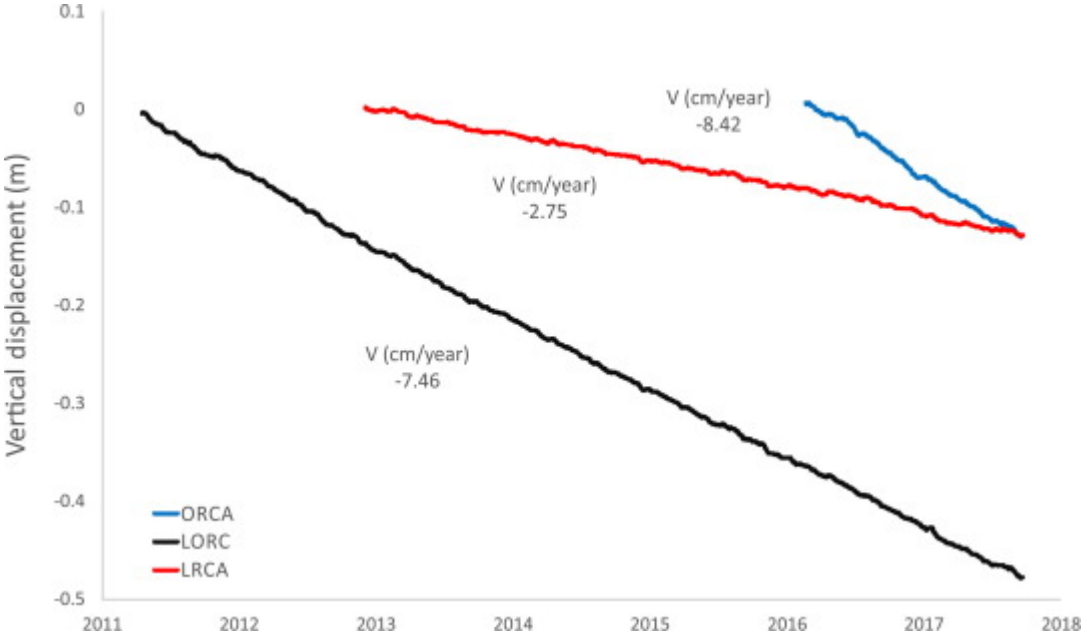

Figure 5: GNSS permanent stations time series.

Subsidence was also observed in the first results of the GNSS campaigns (Tab. 2). All the observed benchmarks located in the basin area present this subsiding pattern, with higher rates in the areas near the subsidence maximum (GNSS2) and slight deformations in the remote ones (GNSS1 and GNSS3).

Table 2: GNSS campaigns results.

GNSS Benchmark	GNSS Campaign Feb 2016-May 2017	
	H (m msl)	V Vert (cm/year)
GNSS1	350.863	−0.5
GNSS2	344.083	−3.8
GNSS3	320.134	−0.1

4.3 Surveying monitoring

The leveling campaign along line 10426 presented in this work and developed in 2016 was compared with that performed by the Spanish National Geographical Institute (IGN) in 2005. Calculated elevations and displacements are showed in Table 5.

Elevations are expressed in meters above mean sea level (msl) and the absence of readings in some benchmarks of the 2005 line means that: the benchmarks were destroyed and replaced (integer kms); or they are new benchmarks for densification of the leveling line in the most subsiding area (medium kms). Benchmarks in km 3 and 4, located in the nearest area to the maximum deformation area show the highest deformation rates, near -10 cm/year, in agreement with InSAR and GNSS measurements.

4.4 Multi-technique comparison and validation

In order to compare both SAR processing and additional data from levelling and GNSS measurements, the different satellites bands and acquisition geometries must be taken into

account. This fact implies that incidence angles are different and LOS displacements should be projected onto the vertical direction. Figure 6 represents the extent of the deformation areas.

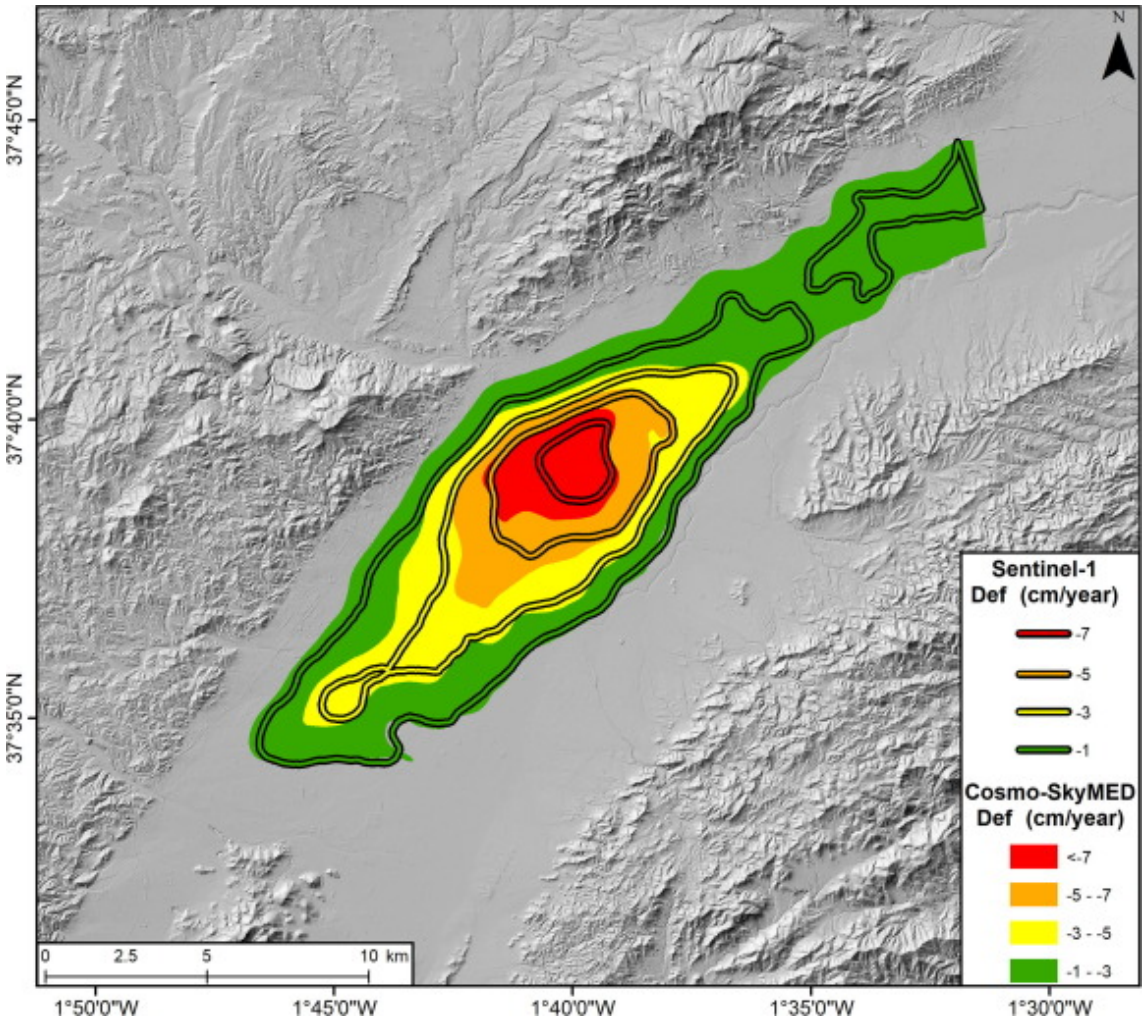

Figure 6: Spatial comparison of the CSK and S-1 vertical deformations. CSK surfaces are represented as poligons and S-1 surfaces as lines allowing to visually compare both deformation patterns.

Spatially, areas between the -3 and -7 cm/year thresholds in S-1 are similar to that defined by CSK results, but deformed areas between the stability threshold (i.e. ±1 cm/year) and -3 cm/year threshold and the maximum subsidence area (>-7 cm/year), increase the difference between them as is shown in Table 3. This difference is higher in the western side of the subsidence bowl while both areas fit well in the eastern side.

Table 3: Deformed areas in CSK and S-1 results.

Subsidence interval (cm/year)	**CSK Deformed Area (km^2)**	**S-1 Deformed Area (km^2)**	**Difference (km^2)**
<−7	11	4	7
−7 to −5	17	14	3
−5 to −3	31	27	4
−3 to −1	71	53	18

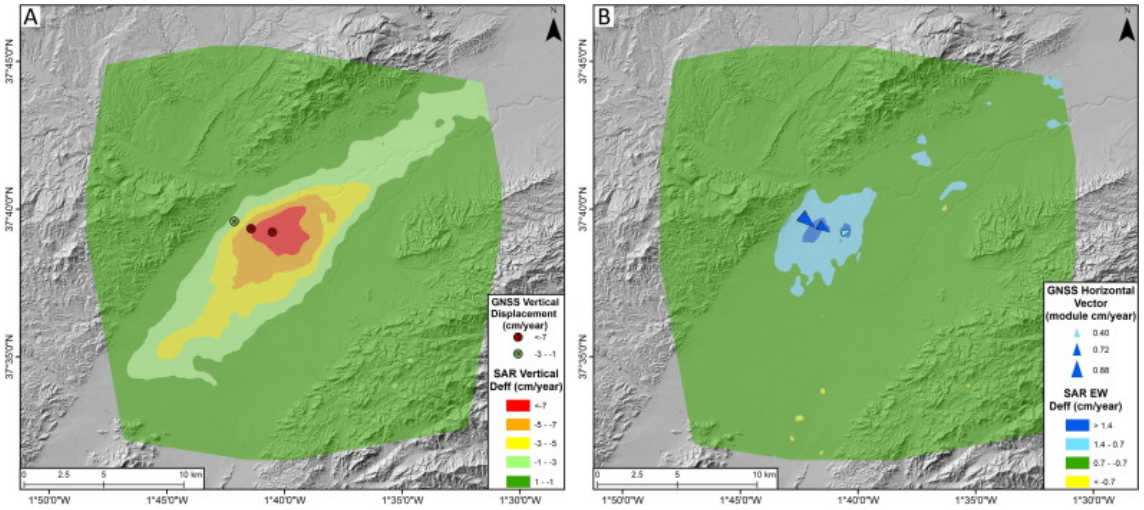

Figure 7: LOS displacement decomposition into Vertical (A) and E-W (B) movements. Points and arrows represent the GNSS permanent stations vertical and horizontal movements, respectively.

Decomposed movements (Fig. 7) revealed an intense vertical ground surface deformation with a maximum value of -9.7 cm/year in the central area of the basin and a good spatial correlation with the GNSS measurements. Total area under the subsidence threshold (±1 cm/year) is around 60 km^2. In the area that shows the highest differences between S-1 and CSK LOS displacements, a maximum horizontal eastward displacement of 1.5 cm/year was detected.

Comparison of the GNSS and InSAR time series was performed using the average time series of the DS located 200 m around the GNSS station, and the 15 days moving average displacements of the GNSS series (Fig. 8). Taking into account that CSK and S-1 are able to detect only a 77% and 71% of the vertical displacement, respectively, due to their incidence angles, InSAR vertical displacements are calculated to allow their comparison with the GNSS measurements. During the analysis the horizontal components were also taken into account to compare the results obtained from both techniques.

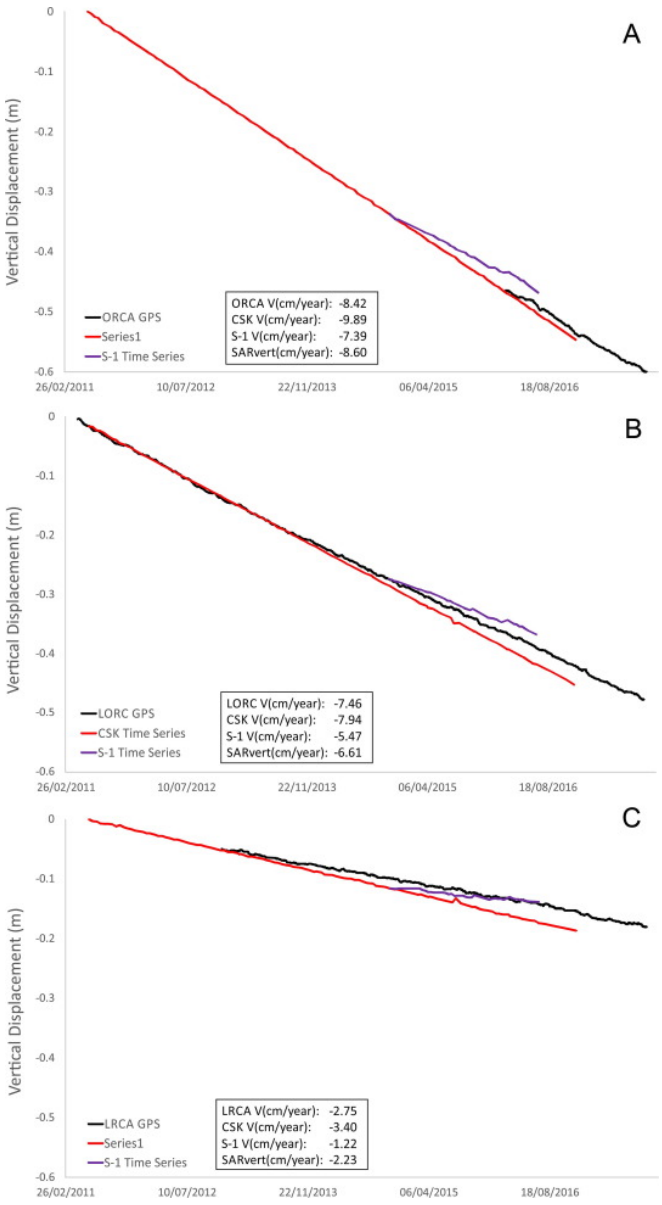

Figure 8: GNSS, CSK and S-1 time series at the ORCA (A), LORC (B) and LRCA (C) GNSS permanent stations.

ORCA station shows the higher GNSS velocities detected, -8.42 cm/year, meanwhile S-1 and CSK velocities at that point are around that velocity, i.e. -7.39 and -9.89 cm/year, respectively. Displacement components calculated in previous section were also compared with GNSS ones, observing a perfect match in vertical velocities (-8.60 cm/year). East-west velocities (Tab. 4) are higher in the SAR results (1.12 cm/year towards E) than GNSS (0.38 cm/year), but confirms a horizontal movement trend in the area (Fig. 8). Note that the common time period at this station is short and velocities can change slightly with longer datasets.

LORC station time series are longer, showing a good fit between CSK and GNSS displacements (-7.94 and -7.46 cm/year, respectively), especially in the first period. In 2014 both time series became to present slightly different trends with higher rates in CSK and lower in S-1 (-5.47 cm/year), with respect to ORCA. During this period decomposed vertical velocity (-6.61 cm/year) is near the GNSS (-6.99 cm/year). The SAR horizontal east-west velocities are around 1.28 cm/year, despite they are over the 0.61 cm/year of the GNSS, the trend towards east is clear.

LRCA station is located near the border of the basin and reveals the lower GNSS velocity (-2.75 cm/year). According with the data of the other stations, S-1 and CSK show velocities around this

value (-1.22 and -3.40 cm/year, respectively) and better accuracy in the vertical decomposed component (-2.23 cm/year). In this case, east-west GNSS movement is 0.68 cm/year and SAR calculated decreases up to 1.21 cm/year.

Table 4: InSAR-GNSS horizontal components of displacement at the GNSS permanent stations. N: norwards; E: eastwards; and U: upwards components of displacement. Note that three displacement values (i.e. vertical and LOS displacements measured from S-1 and CSK) are provided for the upwards (U) component.

		GNSS (cm/year)	**SAR (cm/year)**	**Difference (cm/year)**
LRCA	N	−0.58	–	–
	E	0.67	1.21	0.54
	U	−2.75	−2.23; −1.22; −3.40	0.52; 1.53; −0.65
LORC	N	−0.39	–	–
	E	0.61	1.28	0.67
	U	−7.46	−6.61; −5.47; −7.94	0.85; 1.99; −0.48
ORCA	N	0.13	–	–
	E	0.38	1.12	0.74
	U	−8.42	−8.60; −7.39; −9.89	−0.18; 1.03; −1.47

SAR-GNSS comparison results show that deformation trends are consistent in all the dataset but the acquisition geometry and the possibility of distortion due to horizontal displacements should be taken into account in the cross-validation. Difference between GNSS and decomposed SAR velocities is below 1 cm/year, in the accuracy range of the SAR results defined in section 4.1.

Leveling campaign of January 2016 allows the calculation of the historical deformation trend from 2005 to 2016. First six years of that period (2005-2011) are out of the data period of this work (2011-2016 for the longest time series) and the displacement behavior during it should be analyzed. Vertical projected CSK velocities were used instead of decomposed vertical component to take advantage of the long CSK data period.

Figure 9 and Table 5 show that the measured benchmarks are in the same ranges than CSK and GNSS deformation. In order to improve the results, 100 m average displacements of the CSK points were calculated at each benchmark. Results from km 9, 10, 12 and 13 located in the southern part of the basin, and Node in the northern, are under the stability threshold either in CSK or in Leveling. Benchmarks km 1, 3, 4 and 6 displacement rates are in the same range but slightly higher in the leveling results than in CSK and GNSS. The deviation in the results will be evaluated in section 5 with the definition of validation degrees.

GNSS campaign measurements in the recently built benchmarks (Fig. 9 and Tab. 2) make possible the comparison and valuation of different techniques in order to optimize the monitoring network. GNSS1 and GNSS3 results are in the stable range meanwhile GNSS2 subsidence, 3 km towards the most depressed area, is significantly higher (-3.8 cm/year). All the areas show deformation rates slightly lower than CSK results. Taking into account that May 2017 GNSS and leveling campaigns are out of the sensing period of continuous GNSS stations and InSAR, their results are not compared with them. Updating of GNSS and InSAR processing and ongoing campaigns will probe the effectiveness of the monitoring techniques based on episodic campaigns.

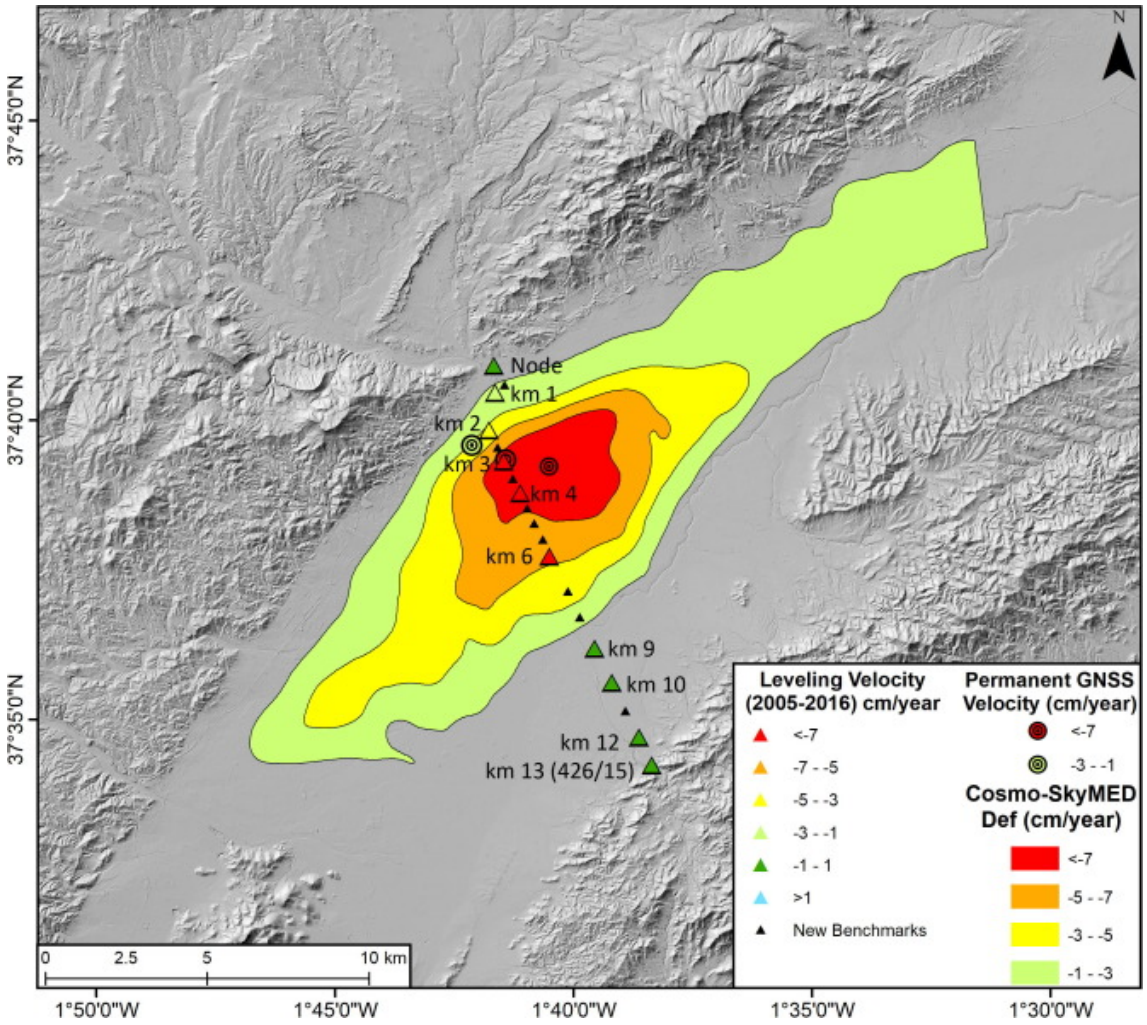

Figure 9: Spatial analysis including CSK, leveling and GNSS results.

Table 5: Leveling benchmarks cumulated displacement. CSK, leveling and GNSS (permanent and campaign) comparison results. Notice the existence of benchmarks with no information due to their renewal or replacement.

	ΔH 2005–2016 (m msl)	**V leveling (cm/year) ΔH/year (2005–2016)**	**2011–2016 V SAR (cm/year)**	**2011–2016 V GNSS (LORC) (cm/year)**	**Difference Leveling - SAR (cm/year)**
km 13		–	0.23	–	–
km 12	−0.021	−0.20	0.22	–	0.44
km 11		–	–	–	–
km 10	−0.041	−0.38	0.36	–	0.74
km 9	−0.082	−0.76	0.16	–	0.92
km 8		–	–	–	–
km 7		–	–	–	–
km 6	−0.822	−7.64	−5.25	–	2.39
km 5.5		–	–	–	–
km 5		–	–	–	–
km 4.5		–	–	–	–
km 4	−1.124	−10.45	−7.66	–	2.79
km 3.5		–	–	–	–
km 3	−1.064	−9.89	−7.95	−7.46	1.94
km 2.5		–	–	–	–
km 2	−0.473	−4.40	–	–	–
km 1	−0.246	−2.29	−1.57	–	0.72
km 0.5		–	–	–	–
Node	−0.086	−0.80	−0.36	–	0.44

Continuous data from three GNSS permanent stations grant a perfect reference point to validate the different techniques. ORCA, LORC and LRCA stations trends and velocities show a good correlation for both CSK and S-1 periods. The trend similarity improves considering the vertical component of the movement (Fig. 7). GNSS horizontal displacements also confirm that, although slower, the eastward deformation trends toward the center of the subsidence are consistent.

Both results highlight the good performance of InSAR. Ground deformation measurements based on episodic campaigns (GNSS and leveling) show the highest divergences. In this case the temporal overlap and scarcity of measurements must be taken into account. The observed divergences illustrate the problem of combining sparse temporal data (leveling, three measurements in 13 years; GNSS campaigns, two measurements in 1.5 years), semi-continuous measurements (CSK, one image each 15 days; S-1, one image each 12 days) and continuous data (GNSS, one day repeatability), especially in cases of non-linear movements.

Table 6: Validation results from full and trend approaches.

		Full Validation		**Trend Validation**	
	Period (years)	**RMSE (cm)**	**Rel. Error (%)**	**V Error (cm/year)**	**Rel. V Error (%)**
LRCA					
S1	1.7	1.27	30.2	1.16	46.1
CSK	4.0	1.73	16.5	0.77	22.7
LORC					
S1	1.7	1.48	12.7	1.36	19.5
CSK	5.5	1.41	3.5	0.60	7.5
ORCA					
S1	0.3	0.49	18.6	2.35	22.8
CSK	0.8	1.12	15.4	1.28	12.2

Full and trend validation approaches were achieved using information from LORC, LRCA and ORCA GNSS stations and InSAR CSK and S-1 data (Tab. 6). Highest RMSE (1.12 - 1.73 cm) are recorded in all the stations for the CSK period in contrast to the percentage error which is lower (3.5 – 16.5%) than S1 (12.7 – 30.2%). This fact introduces the key effect of the evaluated period length. Long periods over 2 years present more stable results either in GNSS or InSAR time series that reduce the relative error. On the other side, short periods (e.g., ORCA) can be affected by punctual trends, distorting the results. Other significant parameter is the relative displacement of the areas; areas with low displacements, near the stability range, are affected by larger relative errors meanwhile highly deformed areas show better results. All this effects are observed in Table 6. LRCA is affected by slight subsidence (around -2.4 cm/year), showing the highest relative error (30.2%) in S1 period (below 2 years). LORC, with high deformation rates (around -7 cm/year) and longer periods, is characterized by lower relative error results (until 3.5%). ORCA station is located in the highest deformation area (around -9 cm/year), but the extremely short measurement period (below 3 months) increases the relative error (between 15.4 and 18.6%). In spite of LRCA-S1 data, full validation results show cumulated errors below 18.6% of total deformation with better correlation in long periods. Trend validation evaluates the trend divergence of data and same conditioning factors than full validation can be observed. Mean velocity trends show that periods over 2 years have errors below 1 cm/year (InSAR

stability threshold). Shorter periods mean velocity errors are near this threshold (except the extremely ORCA-S1 period) reinforcing the full validation interpretation.

Trend comparison includes the comparison of mean velocities from GNSS stations series, InSAR data and leveling campaigns (Table 6) without considering the temporal span. Subsidence velocities derived from leveling measurement (2005-2016) are consistently higher (between 0.44 and 2.79 cm/year) than the CSK results (2011-2016). This divergence can be explained with the data provided by Bonì et al. (2015) where LORC station in the 2007-2009 period had an average velocity of -10.4 cm/year, a velocity decreasing trend also confirmed with the 2011-2016 LORC station data previously presented (-7.46 cm/year). In spite of the mentioned problems, leveling measurements are coherent with the subsidence rates measured with ENVISAT and GNSS permanent stations in the 2003-2010 period.

Leveling and GNSS campaigns developed in 2017 are out of the SAR coverage, preventing the correct comparison of the results of the different techniques. New ongoing campaigns and the extension of the S-1 dataset will allow to improve the analysis of the monitoring system performance and valuate the continuity of the different techniques.

4.5 Upgraded groundwater model

In order to upgrade the empirical formulation, the improved spatial definition of the compressible soils thickness (Bejar-Pizarro et al., 2016) has been introduced in the models, calculating several linear and non-linear empirical models to find the best fit. This updated formulation, obtained from the stress-strain relationship in the period 1992-2010, shows a strong relation between deformation, groundwater changes and compressible thickness. ERS 1/2 data (Fig. 10A) shows a good fit (R^2= 0.863) to an X=0.982·Y regression line (observed-calculated plot). Calculated and observed results also show a good fitting in the deformation-water change plot. ENVISAT results (Fig. 10B) present a better fit (R^2=0.966) to the X=1.02·Y regression line with similar results in the other plot. For both datasets the relationship shown in (7) provides the optimal relationship among the three considered variables:

$$\text{InSAR displacement} = \alpha \times \text{Water Change} \times \text{Compressible Thickness} \quad (7)$$

with α-values of 0.3 and 0.2 for the ERS 1/2 and ENVISAT, respectively.

This new deformation model is used to estimate surface displacements in the period 2012-2016 using the groundwater results derived for this period.

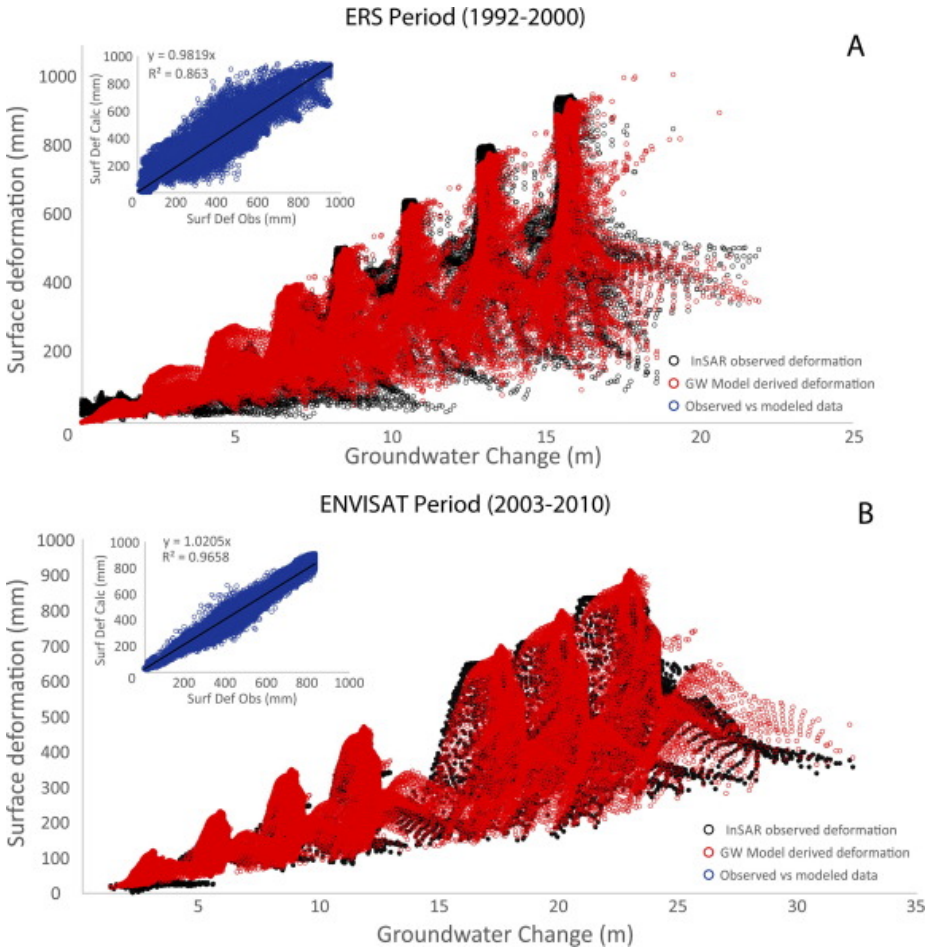

Figure 10: A) Observed and calculated deformation vs. groundwater change in the ERS 1/2 period (1992-2000). B) Observed and calculated deformation vs. groundwater change in the ENVISAT period (2003-2010). In A and B the small plot shows the observed/calculated regression line and R^2.

Since real pumped volume is unavailable, in the first groundwater model calculation (uncalibrated) for 2012-2016 period we use continuous extraction rates of 43 hm^3 from latest available data in the 1960-2012 model. Model results revealed a groundwater level decrease of 67 m (Fig. 11A) with maximum values in the northern area. Predicted surface displacements (Fig. 11C) from calculated water changes generates maximum deformation of more than 1 m with a general deformation over 30 cm (red points, Fig. 11C) covering large areas of the basin.

Taking into account that observed CSK displacement data for the 2012-2016 period (Fig. 3) show maximum displacements of 41 cm with displacements over 30 cm limited to a small area in the basin center, medium-high extraction rates of this model and scarcity of rainfall generated a high decrease of the groundwater that led to an overrated deformation. This mismatch suggests a change in the boundary conditions with respect to the previous periods, which can only be related to pumping rates.

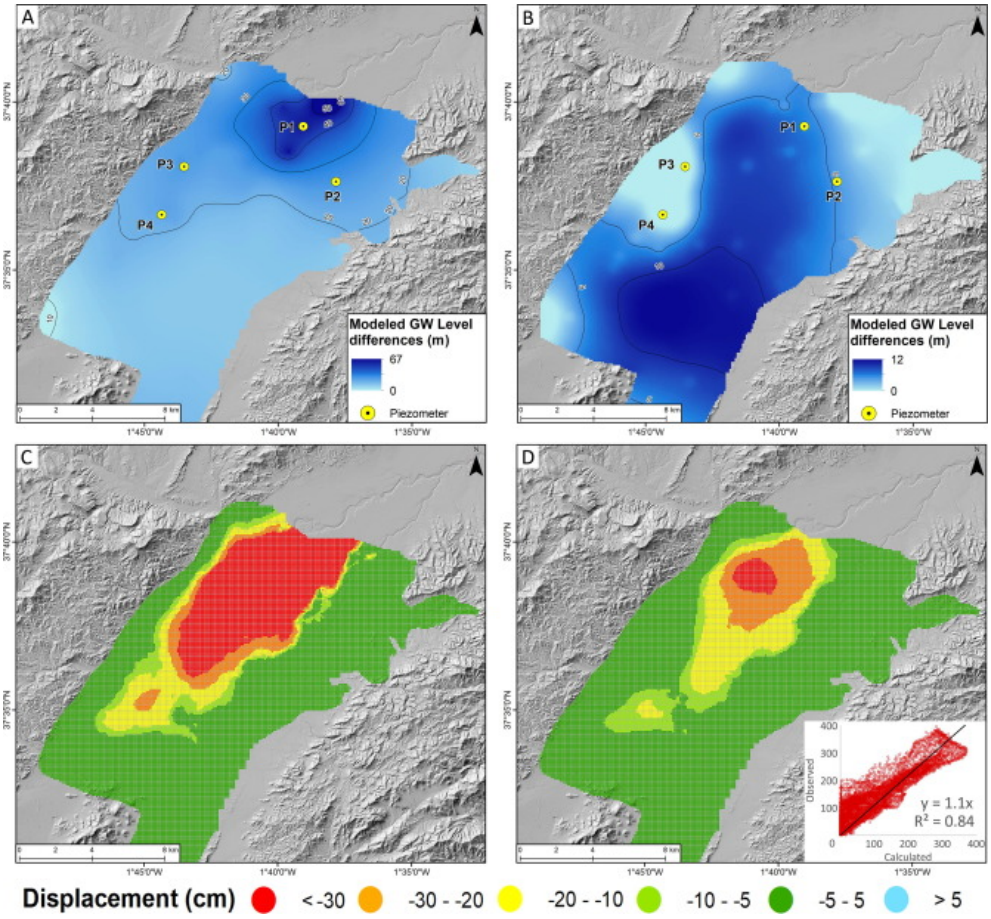

Figure 11: A) 2012-2016 Groundwater level difference obtained using the uncalibrated pumping pressure. B) 2012-2016 groundwater level difference obtained using SAR deformation to calibrate the extracted water. C) Accumulated deformation values calculated using groundwater changes modeled with uncalibrated pumping rates. D) Accumulated deformation values calculated using groundwater changes modeled with the calibrated pumping rates.

After that, new groundwater model calculations were carried out calibrating the pumping rates in order to obtain groundwater levels and deformation results in agreement with the satellite and piezometric measurements. Several pumping rates were introduced to groundwater model using different estimations based on maximum/minimum extraction/rainfall time series. Selected results minimize the difference between the groundwater level and deformation model results and piezometric and InSAR data. Final pumping rates show volumes in the range of previous periods, between 22.6 to 34.6 hm^3 and, also inversely correlated with the yearly accumulated rainfall. In opposition to the uncalibrated model results, the calibrated model piezometry shows a slight groundwater level decrease, below 12 m, distributed over the basin center (Fig. 11B). Calculated displacements generate a subsidence pattern near the CSK results with a maximum deformation of 37 cm (Fig. 11D).

5 Discussion

The Alto Guadalentín basin is being affected by a complex subsidence phenomenon caused by the consolidation of the alternation of the aquifer-system layers, which exhibit different mechanical behaviors, due to the temporal change of groundwater levels. The multi-technique approach presented in this work allows taking advantage of the best characteristic of each monitoring technique, but generates slight divergences in the results that should be analyzed and discussed.

Spatial differences between CSK and S-1 results are located near the Lorca city area, in the west border of the basin. The main difference between both sides of the basin is due to the proximity to the near ranges and the concentration of higher deformable sediments thickness toward that area. That generates high deformation velocities and gradients making the area prone to tensile stresses deriving in horizontal displacements (Feifei et al., 2014). Another portion with horizontal deformations is located in the linking area between the Alto and Bajo Guadalentín basins, here the deformation results are close to the stability threshold and slight changes in the deformation rates have high influence in the results.

S-1 and CSK results present slight differences, which could be attributable to the distinct satellite band, geometry acquisition and the processed time-span period, but both can be used for advanced analysis. Spatial location of the divergence between CSK (ascending) and S-1 (descending) results led to the conclusion that small horizontal displacements could be happening, affecting the results. Horizontal deformation towards east in this area was observed by Fernandez et al. (2018) by means of GNSS campaigns (0.5 - 0.9 cm/year) and S-1 data (1.0 - 1.5 cm/year), and is confirmed in this work when the vertical and E-W components of the displacement are calculated (0.7 - 1.5 cm/year). Vertical movements are consistently measured around -8.5 – -9.0 cm/year in both Fernandez et al., 2018 and current works with all the applied techniques. The significant E-W component in the eastern side of the basin fits with the area were differences between S-1 and CSK, and deformation gradient were higher, suggesting that lateral stresses could be playing an important role in this area. Our results agree with the vertical and horizontal deformation field calculated by Fernandez et al. (2018) with GNSS showing the west side of the basin affected by the strongest horizontal movements toward the deformation maximum. On the other hand, our InSAR results suggest a concentration of horizontal displacement in the western side of the basin meanwhile previous InSAR works (Fernandez et al., 2018) locate this eastward movement in the basin center.

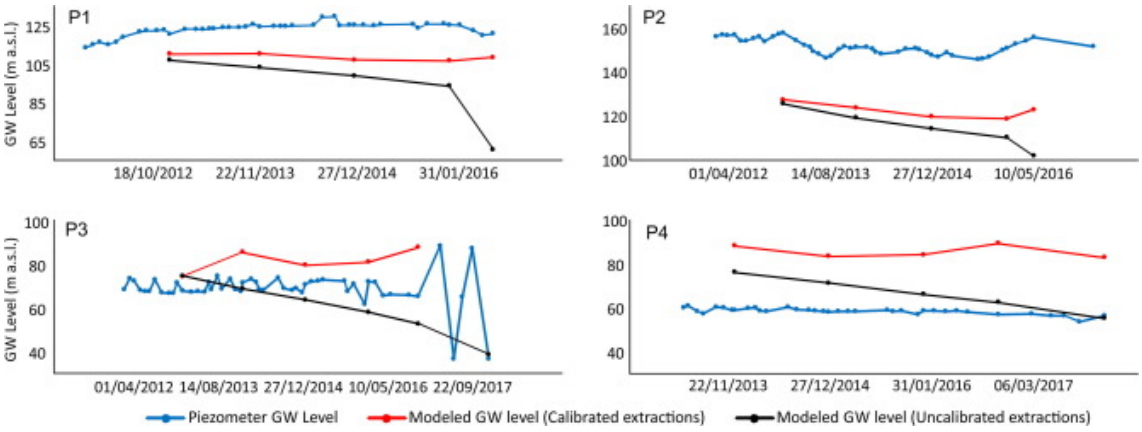

Figure 12: Piezometric measurements and modeled groundwater levels at the available points.

Validation of the calibrated extractions should be done using the limited piezometric data available for the 2012-2017 period. Groundwater data (Fig. 12) show a near stable level between 60 and 150 m msl validating the stable trends calculated with the calibrated model.

The importance of the monitoring system deployed in the basin is related to the further use of the results obtained. The inclusion of the InSAR data, validated in the previous analysis, as a reference layer able to improve the management possibilities of the aquifer-system highlights the progress of the technique.

The new 2012-2017 monitoring period required to update the groundwater model to cover it. The lack of pumping ratios led to use extrapolated data from 1960-2012 period. These uncalibrated water extractions (216.5 hm^3) generate a declining groundwater level, exacerbated by the unfavorable climatic conditions, that result in an estimated surface deformation

extending over a large area with extreme accumulated subsidence above 1 m. Comparing the deformation results with CSK displacements and piezometric stable data, different pumping ratios were proposed. Final calibrated pumping rates present a lower extraction volume (145.9 hm^3) with rational extractions related to the available surficial water that generate slow changes in the groundwater levels, following the trends showed by the piezometric data (Fig. 12). Maximum estimated deformation for the calibrated results is around -37 cm in a small area of the basin center showing a good agreement with the deformations measured by CSK (R^2=0.84).

The lack of extraction data made the comparison between piezometric data and groundwater model output the only available validation. Aquifer-system levels have remained near-stable during the last 5 year in the available piezometers, as seen in figure 12. Model results (calibrated extractions) for the same period show the same near-stable trends supporting its better performance during the 2012-2016 period than those from uncalibrated extractions. Water depth differences are an inherit problem from previous model results, calibrated with scarce piezometric information in the last period (see Ezquerro et al., 2017 for more information). In spite of these problems, the results probe the proficiency of the methodology to use InSAR displacements as an input data to derive groundwater information. New data will allow the future improvement of the complete model.

6 Conclusions

Sustainable and efficient aquifer-systems management in arid areas is one of the most important challenge in groundwater field. Difficulties in knowledge of the groundwater masses health due to sparse and expensive methods like piezometric wells are now supported by new InSAR high density measurements and coupled deformation models.

We have used satellite and geodetic techniques to improve the monitoring of a basin affected by the largest land subsidence due to groundwater extraction in Europe. InSAR measurements from CSK and Sentinel-1 satellites confirmed that the subsidence trend described in previous studies (-10 – -12 cm/year), continues slightly attenuated, in the present (-8 – -9 cm/year). Using ascending (CSK) and descending (S-1) satellite geometries allowed to decompose the deformation field (Up-Down, E-W) showing a slow but clear horizontal deformation towards the basin center in its western side. Continuous data from GNSS stations has confirmed the existence of that trend. These data were also used to validate the vertical deformation results obtaining good correlation with RMSE around 1.5 cm. relative errors that only reach 3 – 30% of it. Analysis of the displacement velocities present comparison results in the stability range of the processing (±1 cm/year).

In order to improve the well-management of aquifer-systems and increase the value of InSAR data for this process, a new methodology was proposed and developed in the Alto Guadalentín basin. Groundwater flow and deformation models generated for the 1960 – 2012 period, have been updated with the latest geological and meteorological information to cover the new 2012 – 2017 InSAR sensing period. Unknown pumping rates of the new period have been calibrated using InSAR deformation, improving a 32% the extracted volumes and demonstrating the good performance of the system.

The results achieved in this study confirms the capability of InSAR measurements to monitor vertical and horizontal surface displacements. They also indicate the high value of this technique, coupled with groundwater flow and geo-mechanical models to generate advanced products of paramount importance for aquifer-systems water management, geohazards monitoring and urban planning.

Acknowledgments

This work was supported by the Spanish Ministry of Economy, Industry and Competitiveness (MINECO), the State Agency of Research (AEI) and European Funds for Regional Development (FEDER), under projects AQUARISK (ESP2013-47780-C2-2-R), TEMUSA (TEC2017-85244-C2-1-P) and STAR-EO (TIN2014-55413-C2-2-P). First author shows gratitude for PhD student contract BES-2014-069076. A first version of this work was written during the research stay of first and third authors in the Università degli Studi di Firenze supported by the Spanish Ministry of Education, Culture and Sport, under fellowships EEBB-I-18-13014 and PRX17/00439, respectively.

Conflicts of interests

The authors declare that there is no conflict of interest regarding the publication of this paper.

Authors Contribution

P.E. and G.H. conceived, coordinated and wrote the manuscript in collaboration with all the coauthors. P.E. processed InSAR data. P.E., R.T, M.B.P. and G.E. analyzed InSAR results. P.E. and C.G.A. generated the hydrogeological models. P.E., J.F.M. and G.E. developed the deformation models. A.S. designed and analyzed levelling and GNSS field campaign. J.A.S.S. processed the GNSS data. All authors were involved in developing the presented ideas and reviewed the manuscript.

7 References

Abidin, H.Z., Gumilar, I., Andreas, H. et al. Environ Earth Sci (2013) 68: 1545. https://doi.org/10.1007/s12665-012-1848-z

Alfarrah, N., K. Walraevens, 2018. Groundwater Overexploitation and Seawater Intrusion in Coastal Areas of Arid and Semi-Arid Regions. Water, 10(2), 143. https://doi.org/10.3390/w10020143

Amelung, F., Galloway, D., Bell, J., Zebker, H., Laczniak, R. 1999. Sensing the ups and downs of Las Vegas: InSAR reveals structural control of land subsidence and aquifer-system deformation. Geology ; 27 (6): 483–486.

Banta, E. R. ModelMate—A Graphical User Interface for Model Analysis: U.S. Geological Survey Techniques and Methods, Book 6, Chap. E4, 31 p., 2011.

Blanco-Sánchez, J., Mallorquí, J., Duque, S., Monells, D., 2008. The Coherent Pixels Technique (CPT): An Advanced DInSAR Technique for Nonlinear Deformation Monitoring. Pure Appl. Geophys. 165, 1167– 1193.

Béjar-Pizarro, M.; Guardiola-Albert, C.; García-Cárdenas, R.P.; Herrera, G.; Barra, A.; López Molina, A.; Tessitore, S.; Staller, A.; Ortega-Becerril, J.A.; García-García, R.P., 2016. Interpolation of GPS and Geological Data Using InSAR Deformation Maps: Method and Application to Land Subsidence in the Alto Guadalentín Aquifer (SE Spain). Remote Sens. 8, 965. https://doi.org/10.3390/rs8110965

Béjar-Pizarro, M.; Notti, D.; Mateos, R.M.; Ezquerro, P.; Centolanza, G.; Herrera, G.; Bru, G.; Sanabria, M.; Solari, L.; Duro, J.; Fernández, J. 2017a. Mapping Vulnerable Urban Areas Affected by Slow-Moving Landslides Using Sentinel-1 InSAR Data. Remote Sens. 2017, 9, 876. https://doi.org/10.3390/rs9090876

Béjar-Pizarro, M., Ezquerro, P., Herrera, G., Tomás, R., Guardiola-Albert, C., Ruiz Hernández, J. M., Fernández Merodo, J. A., Marchamalo, M., Martínez, R. 2017b. Mapping groundwater level and aquifer storage variations from InSAR measurements in the Madrid aquifer, Central Spain, Journal of Hydrology, Volume 547, 2017, Pages 678-689, ISSN 0022-1694, https://doi.org/10.1016/j.jhydrol.2017.02.011

Bonì, R., Herrera, G., Meisina, C., Notti, D., Béjar-Pizarro, M., Zucca, F., González, P. J., Palano, M., Tomás, R., Fernández, J., Fernández-Merodo, J. A., Mulas, J., Aragón, R., Guardiola-Albert, C., Mora, O., 2015. Twenty-year advanced DInSAR analysis of severe land subsidence: the Alto Guadalentín Basin (Spain) case study. Eng. Geology. http://doi.org/10.1016/j.enggeo.2015.08.014

Bonì, R., Cigna, F., Bricker, S., Meisina, C., McCormack, H. 2016. Characterisation of hydraulic head changes and aquifer properties in the London Basin using Persistent Scatterer Interferometry ground motion data, Journal of Hydrology, Volume 540, 2016, Pages 835-849, ISSN 0022-1694, https://doi.org/10.1016/j.jhydrol.2016.06.068.

Bozzano, F., Esposito, C., Franchi, S., Mazzanti, P., Perissin, D., Rocca, A., Romano, E., 2015. Understanding the subsidence process of a quaternary plain by combining geological and hydrogeological modelling with satellite InSAR data: The Acque Albule Plain case study. Remote Sensing of Environment, Vol 168, pp 219-238, ISSN 0034-4257, http://doi.org/10.1016/j.rse.2015.07.010.

Centolanza, G., Duro, J., Mallorquí, J.J., 2017. Achieving precise Sentinel 1 coregistration with CPT, experience and lesson learnt. In Proceedings of the Fringe 2017 Workshop, Helsinky, Finland, 5–9 June 2017.

Cerón, J.C., and Pulido-Bosch, A., 1996. Groundwater problems resulting from CO2 pollution and overexploitation in Alto Guadalentín aquifer (Murcia, Spain). Environmental Geology, 28 (4) 223–228. http://doi.org/10.1007/s002540050096

Cerón, J.C., 1995. Estudio hidrogeoquímico del acuífero del Alto Guadalentín (Murcia) [Ph.D. thesis]: Granada, University of Granada, pp. 265

Chaussard, E., Wdowinski, E., Cabral-Cano, E., Amelung, F., 2014a. Land subsidence in central Mexico detected by ALOS InSAR time-series. Remote Sensing of Environment, Volume 140, pp 94-106, https://doi.org/10.1016/j.rse.2013.08.038

Chaussard, E., R. Bürgmann, M. Shirzaei, E. J. Fielding, and B. Baker. 2014b. Predictability of hydraulic head changes and characterization of aquifer-system and fault properties from InSAR-derived ground deformation, J. Geophys. Res. Solid Earth, 119, 6572–6590, doi: 10.1002/2014JB011266.

Chen, M., Tomás, R., Li, Z., Motagh, M., Li, T., Hu, L., Gong, H., Li, X., Yu, J. & Gong, X. 2016a. Imaging Land Subsidence Induced by Groundwater Extraction in Beijing (China) Using Satellite Radar Interferometry. Remote Sensing, 8, 468, doi: https://doi.org/10.3390/rs8060468.

Chen, J., R. Knight, H. A. Zebker, and W. A. Schreuder (2016b), Confined aquifer head measurements and storage properties in the San Luis Valley, Colorado, from spaceborne InSAR observations, Water Resour. Res., 52, doi: 10.1002/2015WR018466.

CHS, 2006. Plan especial ante situaciones de alerta y eventual sequía en la cuenca del Segura: 238 Confederación hidrográfica del Segura, Tech. rep., 298 p., 239.

CHS, 2014. Plan Hidrológico de la Cuenca del Segura 2015/2021. Análisis piezométrico histórico y de los últimos 25 años (1990-2014) de las masas de Agua subterráneas de la demarcación Hidrográfica del Segura. 070.057 Alto Guadalentín. Tech. rep. http://www.chsegura.es/chs/cuenca/sequias/pes/eeapes.html#doc_completa

Confuorto, P., Di Martire, D., Centolanza, G., Iglesias, R., Mallorqui, J.J., Novellino, A., Plank, S., Ramondini, M., Thuro, K., Calcaterra, D., 2017. Post-failure evolution analysis of a rainfall-triggered landslide by multi-temporal interferometry SAR approaches integrated with geotechnical analysis. Remote Sens. Environ. 188, 51–72, https://doi.org/10.1016/j.rse.2016.11.002.

Covello, F., F. Battazza, A. Coletta, E. Lopinto, C. Fiorentino, L. Pietranera, G. Valentini, S. Zoffoli, 2010. COSMO-SkyMed an existing opportunity for observing the Earth. Journal of Geodynamics, Vol 49, 3–4, pp 171-180, https://doi.org/10.1016/j.jog.2010.01.001

Dach, R., S. Lutz, P. Walser, P. Fridez (Eds), 2015: Bernese GNSS Software Version 5.2. User manual, Astronomical Institute, University of Bern, Bern Open Publishing. https://doi.org/10.7892/boris.72297

Del Soldato, M., Farolfi, G., Rosi, A., Raspini, F. & Casagli, N. 2018. Subsidence Evolution of the Firenze–Prato–Pistoia Plain (Central Italy) Combining PSI and GNSS Data. Remote Sensing, 10, 1146.

Densmore, J.N., Woolfenden L.R., Rewis, D.L., Martin, P.M., Sneed, M., Ellett, K.M., Solt, M., and Miller, D.M., 2018, Geohydrology, geochemistry, and numerical simulation of groundwater flow and land subsidence in the Bicycle Basin, Fort Irwin National Training Center, California: U.S. Geological Survey Scientific Investigations Report 2018–5067, 176 p., https://doi.org/10.3133/sir20185067.

Dow, J.M., R. E. Neilan, C. Rizos (2009). "The International GNSS Service in a changing landscape of Global Navigation Satellite Systems", Journal of Geodesy. vol. 83, pp 191–198, https://doi.org/10.1007/s00190-008-0300-3

European Union. Science for Water. European Commission Joint Research Centre (JRC) thematic report. Available at: https://ec.europa.eu/jrc/en/publication/thematicreports/ science-water (Date of access: 20th April 2017).

Erkens, J., T. Bucx, R. Dam, G. de Lange and J. Lambert, 2015. Sinking coastal cities. Proc. IAHS, 372, 189–198. https://doi.org/10.5194/piahs-372-189-2015

ESA S-1 IW User guide, https://sentinel.esa.int/web/sentinel/user-guides/sentinel-1-sar/acquisition-modes/interferometric-wide-swath

Ezquerro, P., Herrera, G., Marchamalo, M., Tomás, R., Béjar-Pizarro, M., Martínez, R. 2014. A quasi-elastic aquifer deformational behavior: Madrid aquifer case study, Journal of Hydrology, Volume 519, Part A, 2014, Pages 1192-1204, ISSN 0022-1694, https://doi.org/10.1016/j.jhydrol.2014.08.040.

Ezquerro, P., Guardiola-Albert, C., Herrera, G., Fernández-Merodo, J.A., Béjar-Pizarro, M., Bonì, M., 2017. Groundwater and subsidence modelling combining geological and multi-satellite SAR data over the Alto Guadalentín aquifer (SE Spain). Geofluids, vol. 2017. https://doi.org/10.1155/2017/1359325.

Feifei, Q., Zhang, Q., Lu, Z., Zhao, C., Yang, C., Zhang, J. 2014.Land subsidence and ground fissures in Xi'an, China 2005–2012 revealed by multi-band InSAR time-series analysis, Remote Sensing of Environment, Volume 155, 2014, Pages 366-376, ISSN 0034-4257, https://doi.org/10.1016/j.rse.2014.09.008.

Fernandez, J., Prieto, J. F., Escayo, J., Camacho, A. G., Luzón, F., Tiampo, K. F., Palano, M., Abajo, T., Pérez, E., Velasco, J., Herrero, T., Bru, G., Molina, I., López, J., Rodríguez-Velasco, G., Gómez, I., Mallorquí, J. J. 2018. Modeling the two- and three-dimensional displacement field in Lorca, Spain, subsidence and the global implications. Scientific Reports, 14782, 8, 1. https://doi.org/10.1038/s41598-018-33128-0

Ge, L., A. Hay-Man Ng, X. Li, H.Z. Abidin, I. Gumilar, 2014. Land subsidence characteristics of Bandung Basin as revealed by ENVISAT ASAR and ALOS PALSAR interferometry. Remote Sensing of Environment, Vol 154, pp 46-60, https://doi.org/10.1016/j.rse.2014.08.004

González, P.J.; Fernández, J., 2011. Drought-driven transient aquifer compaction imaged using multitemporal satellite radar interferometry. Geology, 39, 551–554. http://doi.org/10.1130/G31900.1

Harbaugh, A.W., 2005. MODFLOW-2005, the U.S. Geological Survey modular ground-water model -- the Ground-Water Flow Process: U.S. Geological Survey Techniques and Methods 6-A16

Herrera, G., Fernández, J. A., Tomás, R., Cooksley, G., and Mulas, J. 2009. Advanced interpretation of subsidence in Murcia (SE Spain) using A-DInSAR data – modelling and validation, Nat. Hazards Earth Syst. Sci., 9, 647-661, https://doi.org/10.5194/nhess-9-647-2009

Hoffmann, J., Zebker, H. A., Galloway, D. L., and Amelung, F. (2001), Seasonal subsidence and rebound in Las Vegas Valley, Nevada, observed by Synthetic Aperture Radar Interferometry, Water Resour. Res., 37(6), 1551– 1566, doi:10.1029/2000WR900404.

Hoffmann, J., Galloway, D.L., Zebker, H.A., 2003. Inverse modeling of interbed storage parameters using land subsidence observations, Antelope Valley, California. Water Resources Research 39, 5–10.

Hu, B., Zhou, J., Wang, J., Chen, Z., Wang, D., Xu, S., 2009. Risk assessment of land subsidence at Tianjin coastal area in China. Environmental Earth Sciences. 59, 2, 269 https://doi.org/10.1007/s12665-009-0024-6

Hu, J., Li, Z.W., Ding, X.L. et al. J Geod (2012) 86: 1029. https://doi.org/10.1007/s00190-012-0563-6

IGME (1985) Mapa Hidrogeológico de España, 1:200.000, Sheet Murcia (79). Servicio de Publicaciones Ministerio de Industria, Madrid. Tech. rep.

IGME, “Estudio para la regulaci´on y apoyo a la gestión de los recursos hídricos subterráneos del Alto Guadalentín (Murcia),” Modelo matemático de flujo subterráneo. IGME internal report ref. 33237, 1994.

Leake, S.A., and Galloway, D.L., 2007, MODFLOW ground-water model—User guide to the Subsidence and Aquifer-System Compaction Package (SUB-WT) for water-table aquifers: U.S. Geological Survey, Techniques and Methods 6–A23, 42 p.

Leick, A, (1995): “GPS Satellite Surveying” (1995), Wiley, ISBN 0-471-30626-6.

Liu, Y., Huang, H-J. 2013. Characterization and mechanism of regional land subsidence in the Yellow River Delta, China. Natural Hazards, 68, pp 687-709, https://doi.org/10.1007/s11069-013-0648-4

Masana, E., J. J. Martínez-Díaz, J. L. Hernández-Enrile, and P. Santanach, 2004. The Alhama de Murcia fault (SE Spain), a seismogenic fault in a diffuse plate boundary: Seismotectonic implications for the Ibero-Magrebian region, J. Geophys. Res., 109, B01301, http://doi.org/10.1029/2002JB002359.

Massonet, D., Feigl, K. L. 1998. Radar Interferometry and its Application to Changes in the Earth’s Surface. Rev. Geophys. 36, 441–500.

Miller, M. M., and M. Shirzaei (2015), Spatiotemporal characterization of land subsidence and uplift in Phoenix using InSAR time series and wavelet transforms, J. Geophys. Res. Solid Earth, 120, 5822–5842, doi: 10.1002/2015JB012017.

Minderhoud, P.S.J., Erkens, G., Pham, V.H., Vuong, B.T., Stouthamer, E., 2015. Assessing the potential of the multi-aquifer subsurface of the Mekong Delta (Vietnam) for land subsidence due to groundwater extraction. Proc. Int. Assoc. Hydrol. Sci., 372, pp. 73-76, https://doi.org/10.5194/piahs-372-73-2015

Mora, O., Mallorquí, J.J., Broquetas, A., 2003. Linear and nonlinear terrain deformation maps from a reduced set of interferometric SAR images. IEEE Trans. Geosci. Remote Sens. 41, 2243–2253.

Motagh, M., T. R. Walter, M. A. Sharifi, E. Fielding, A. Schenk, J. Anderssohn, and J. Zschau, 2008. Land subsidence in Iran caused by widespread water reservoir overexploitation, Geophys. Res. Lett., 35, L16403, https://doi.org/10.1029/2008GL033814

Notti, D.; Herrera, G.; Bianchini, S.; Meisina, C.; García-Davalillo, J.C.; Zucca, F. A, 2014. Methodology for improving landslide PSI data analysis. Int. J. Remote Sens. 35, 2186–2214

Ochoa-González, G.H., Carreón-Freyre, D., Franceschini, A., Cerca, M., Teatini, P. 2018. Overexploitation of groundwater resources in the faulted basin of Querétaro, Mexico: A 3D deformation and stress analysis, Engineering Geology, Volume 245, 2018, Pages 192-206, ISSN 0013-7952, https://doi.org/10.1016/j.enggeo.2018.08.014.

Poeter, E. P., Hill, M. C., Lu, D., Tiedeman, C. R. and Mehl, S. "UCODE 2014, with new capabilities to define parameters unique to predictions , calculate weights using simulated values, estimate parameters with SVD, evaluate uncertainty with MCMC, and More: Integrated Groundwater Modeling Center Report Number: GWMI 2014-02," GWMI, 2014.

Raspini, F.; Cigna, F.; Moretti, S., 2012. Multi-Temporal Mapping of Land Subsidence at Basin Scale Exploiting Persistent Scatterer Interferometry: Case Study of Gioia Tauro Plain (Italy). J. Maps. https://doi.org/10.1080/17445647.2012.743440

Raspini, F., C. Loupasakis, D. Rozos, and S. Moretti, 2013. Advanced interpretation of land subsidence by validating multi-interferometric SAR data: the case study of the Anthemountas basin (Northern Greece). Nat. Hazards Earth Syst. Sci., 13, 2425–2440. https://doi.org/10.5194/nhess-13-2425-2013

Righini, G., Raspini, F., Moretti, S., & Cigna, F. (2011). Unsustainable use of groundwater resources in agricultural and urban areas: a persistent scatterer study of land subsidence at the basin scale. WIT Transactions on Ecology and the Environment, 144(544), 81-92

Rigo, A., Béjar-Pizarro, M., Martínez-Díaz, J., 2013. Monitoring of Guadalentín valley (southern Spain) through a fast SAR Interferometry method. J. Appl. Geophys. 91, 39-48. http://doi.org/10.1016/j.jappgeo.2013.02.001

Riley, F. S., 1969, Analysis of borehole extensometer data from central California, in Tison, L. J., éd., Land subsidence, v. 2: International Association of Scientific Hydrology Publication 89, p. 423-431

Solari, L., Del Soldato, M., Bianchini, S., Ciampalini, A., Ezquerro, P., Montalti, R., ... & Moretti, S. (2018). From ERS 1/2 to Sentinel-1: subsidence monitoring in Italy in the last two decades. Frontiers in Earth Science, 6, 149.

Teatini, P., Ferronato, M., Gambolati, G., Bertoni, W., Gonella, M. 2005. A century of land subsidence in Ravena, Italy. Enviromental Geology, 47, pp 831-846, https://doi.org/10.1007/s00254-004-1215-9

Teatini, P., Ferronato, M., Gambolati, G., 2006. Groundwater pumping and land subsidence in the Emilia-Romagna coastland, Italy: Modeling the past occurrence and the future trend. Water Resources Research. Vol. 42. https://doi.org/10.1029/2005WR004242

Terzaghi, K., 1925. Settlement and Consolidation of Clay. McGraw-Hill, New York, pp. 874–878.

Tessitore, S., Fernández-Merodo, J.A., Herrera, G. et al. Hydrogeol J (2016) 24: 727. https://doi.org/10.1007/s10040-015-1349-8

Tomas, R., Herrera, G., Lopez-Sanchez, J.M., Vicente, F., Cuenca, A., Mallorquí, J.J. 2010. Study of the land subsidence in Orihuela City (SE Spain) using PSI data: Distribution, evolution and correlation with conditioning and triggering factors, Engineering Geology, Volume 115, Issues 1–2, 2010, Pages 105-121, ISSN 0013-7952, https://doi.org/10.1016/j.enggeo.2010.06.004

Tomas, R., Herrera, G., Cooksley, G., Mulas, G., 2011. Persistent Scatterer Interferometry subsidence data exploitation using spatial tools: The Vega Media of the Segura River Basin case study. Journal of Hydrology. 400, 411-428. https://doi.org/10.1016/j.jhydrol.2011.01.057

Tomás, R., Romero, R., Mulas, J., Marturià, J.J., Mallorquí, J.J., Lopez-Sanchez, J.M., Herrera, G., Gutiérrez, F., González, P.J., Fernández, J., Duque, S., Concha-Dimas, A., Cocksley, G., Castañeda, C., Carrasco, D. & Blanco, P. 2014. Radar interferometry techniques for the study of ground subsidence phenomena: a review of practical issues through cases in Spain. Environmental Earth Sciences, 71, 163-181, https://doi.org/10.1007/s12665-013-2422-z

Torres, R., Snoeij, P., Geudtner, D., Bibby, D., Davidson, M., Attema, E., Potin, P., Rommen, B., Floury, N., Brown, M., Navas, I., Deghaye, P., Duesmann, B., Rosich, B., Miranda, N., Bruno, C., L'Abbate, M., Croci, R., Pietropaolo, A., Huchler, M., Rostan, F., 2012. GMES Sentinel-1 mission. Remote Sensing of Environment, Vol 120, pp 9-24, https://doi.org/10.1016/j.rse.2011.05.028

Vousdoukas, M. I., Mentaschi, L., Voukouvalas, E. , Verlaan, M. and Feyen, L., 2017, Extreme sea levels on the rise along Europe's coasts. Earth's Future, 5: 304-323. https://doi.org/10.1002/2016EF000505

Wada, Y., Bierkens, M.F.P., 2014. Sustainability of global water use: past reconstruction and future projections. Environ. Res. Lett. 9. https://doi.org/10.1088/1748-9326/9/10/104003

Winston, R. B. “ModelMuse-A graphical user interface for MODFLOW-2005 and PHAST,” U.S. Geological Survey Techniques and Methods 6-A29, 52 pages, 2009.

Zhang, Y., Gong, H., Gu, Z., Wang, R., Xiaojuan, L., Zhao, W., 2014. Characterization of land subsidence induced by groundwater withdrawals in the plain of Beijing city, China. Hydrogeol J 22: 397. https://doi.org/10.1007/s10040-013-1069-x

Appendix A. Supplementary material

The following are the Supplementary data to this article:

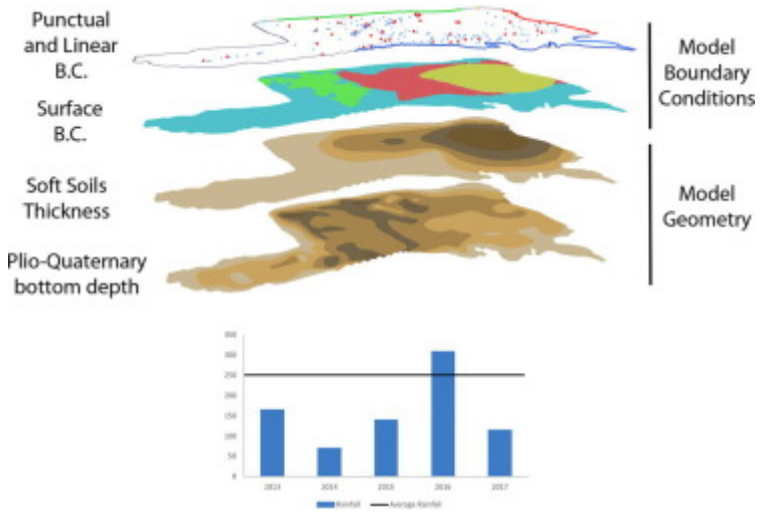

Supplementary figure 1. Groundwater model structure and 950 2013-2017 rainfall data

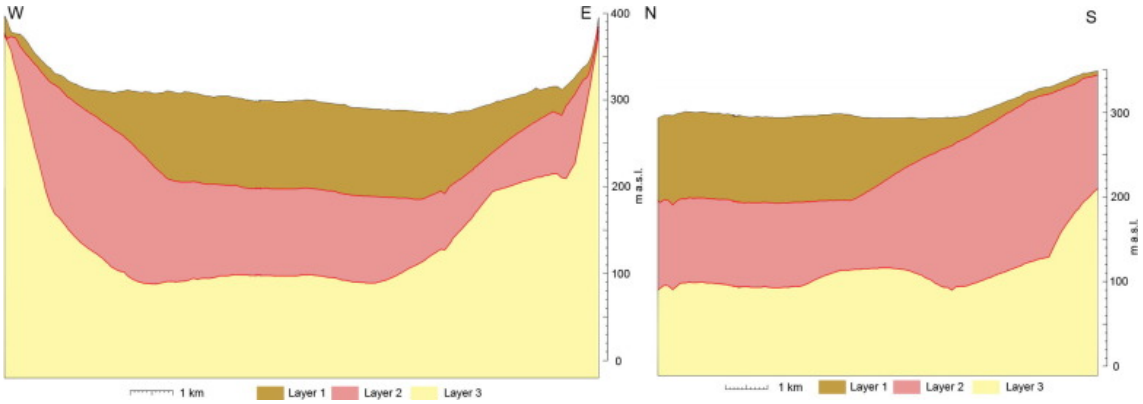

Supplementary figure 2. E-W and N-S Cross-sections of the groundwater model. Layer 1 includes the compressible fine-grained Plio-Quaternary materials. Layer 2 is formed by coarse-grained Plio- Quaternary sediments, representing the main aquifer layer. Layer 3 comprises Miocene low permeability material

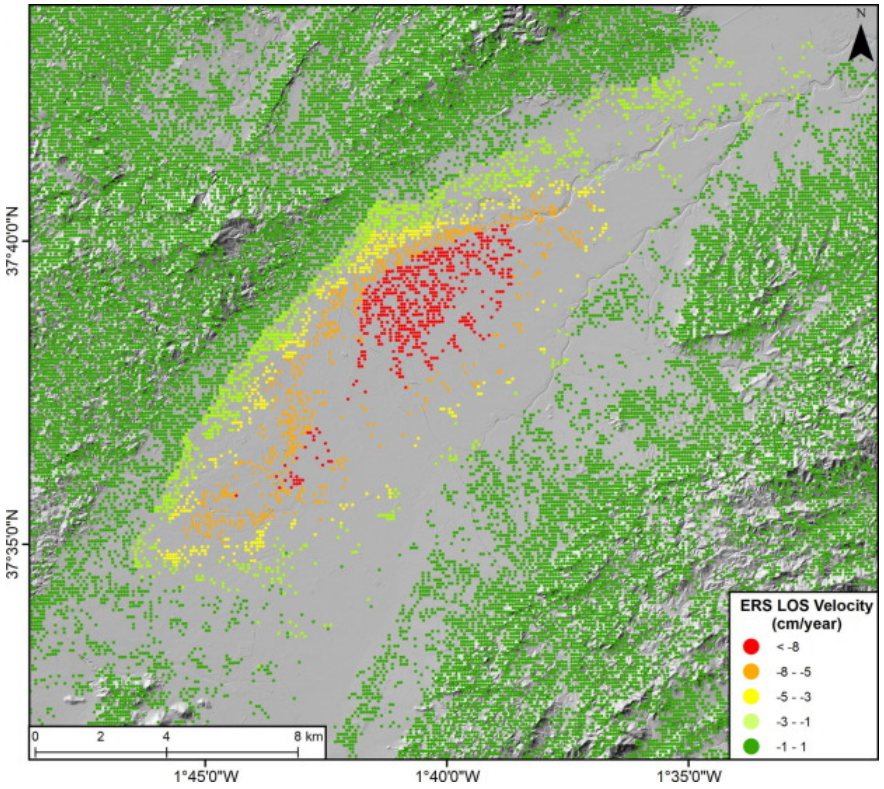

Supplementary figure 3. ERS LOS results (1992-2000)

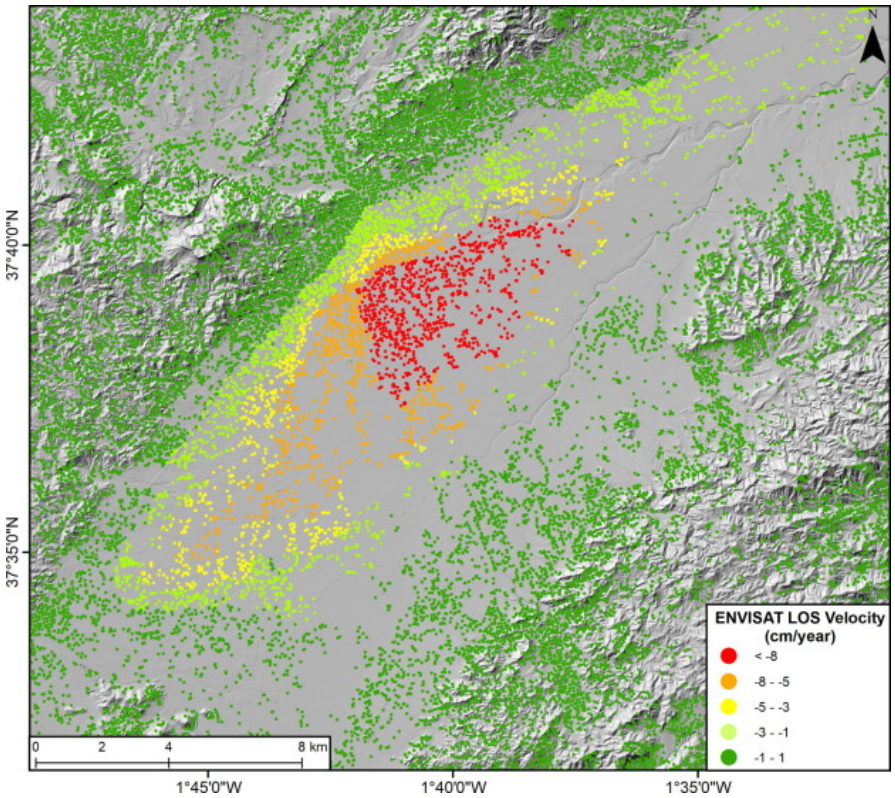

Supplementary figure 4. ENVISAT LOS results (2003-2010)